NTNU

Norwegian University of
Science and Technology

# Formation of intermediate bands in silicon by transition metal doping

A DFT/DFTB computational study

**Kenny Solevåg-Hoti**

Master of Science
Submission date: June 2016
Supervisor: Jon Andreas Støvneng, IFY
Co-supervisor: Turid Reenaas, IFY

Norwegian University of Science and Technology
Department of Physics

*dedicated to my wife, and our future children.*

# Abstract

The intermediate band solar cell offers the possibility of increasing the efficiency of modern-day solar cells. By having a narrow intermediate band placed in the conventional band gap, sequential absorption of photons is attainable. With suitable extraction of charge carriers, the photocurrent can increase whilst the voltage is preserved, leading to higher efficiencies. By using electronic structure calculations within density functional theory (DFT) and density-functional tight-binding (DFTB), we study the possible formation of intermediate bands when silicon is doped with a transition metal impurity. We particularly consider the $4d$ transition metal silver, but also investigate doping by transition metals of the $3d$ series V, Cr, Mn, Fe and Co. We employ density functional theory in the Kohn-Sham approach, using mainly the Perdew-Wang exchange-correlation functional (PW91) within the generalized gradient approximation. Both DFT and DFTB calculations are performed by using modeling suites in the Amsterdam density functional (ADF) package. It is found, by method of DFTB, that substitutional doping of bulk Si with silver at $0.4\%$ impurity concentration, exhibits an intermediate band at the Fermi level, 0.28 eV above the valence band edge. However, it is also found that our DFTB calculations have poor accuracy, and that this result should be cross-examined by a more accurate method. DFT calculations reveals only contours of formation, yet no intermediate bands are found in silicon with silver impurity concentrations down to $6.25\%$. Doping with $3d$ transition metals at $6.25\%$ impurity concentration do not display fully formed intermediate bands.

# Sammendrag

Mellombånd solceller gir muligheten for å øke effektiviteten hos dagens solceller. Ved å ha et mellombånd plassert i det konvensjonelle båndgapet, er sekvensiell absorpsjon av fotoner mulig. Ved egnet ekstraksjon av ladningsbærere kan den lysgenererte strømmen øke, imens spenningen er vedlikeholdt, og økt effektivitet kan oppnås. Ved å bruke elektronisk struktur beregninger innen tetthetsfunksjonalteori (DFT) og tetthetsfunksjonal tettbinding (DFTB), studerer vi mulig formasjon av mellombånd når silisium dopes med overgangsmetallurenheter. Vi fokuserer fortrinnsvis på $4d$ overgangsmetallet sølv, men undersøker også doping ved hjelp av $3d$ overgangsmetall serien V, Cr, Mn, Fe og Co. Vi tar i bruk tetthetsfunksjonalteori på Kohn-Sham tilnærmingsmåten, og bruker i hovedsak Perdew-Wang utvekslings-korrelasjons funskjonalet (PW91) i den generaliserte gradient approksimasjonen. Både DFT og DFTB beregningene gjennomføres i modelleringsdeler av Amsterdam tetthetsfunksjonal (ADF) pakken. Det er funnet, ved metoden DFTB, at substitusjonell doping av bulk Si med sølv ved $0.4\%$ urenhetkonsentrasjon, viser et mellombånd ved Fermi nivået, 0.28 eV over valensbåndkanten. Det er også funnet at våre DFTB beregninger har dårlig nøyaktighet og at resultatet vårt burde bli kryssundersøkt av en mer nøyaktig metode. DFT beregningene synliggjør bare konturene av formasjon, likevel er ingen mellombånd funnet i silisium ved sølv urenhetkonsentrasjon ned til $6.25\%$. Doping med $3d$ overgangsmetaller ved $6.25\%$ urenhetkonsentrasjon viser ingen mellombånd som fullstendig dannet.

# Preface

This thesis marks the end of my studies within the Natural Science with Teacher Education (LUR) master's degree program at the Norwegian University of Science and Technology (NTNU) in Trondheim. The thesis is a 30 points work, and the work has been carried out over the fall semester of 2015 and spring semester of 2016. The objective of this project has been to investigate possible candidate materials for intermediate band solar cells, by method of density functional theory and density-functional tight-binding. More specifically, transition metal doping of silicon has been investigated in the quest of finding formation of intermediate bands. The idea behind the project is attributed to my co-supervisor, Assoc. Professor Turid Worren Reenaas, and the computational work has been made possible by the aid of my supervisor, Assoc. Professor Jon Andreas Støvneng.

## Acknowledgements

I would like to express my deep gratitude to my project supervisors, Prof. Jon Andreas Støvneng and Prof. Turid Worren Reenaas, for their valuable help in the planning and development of this research work. Their useful critiques and willingness to give their time so generously has been greatly appreciated. My grateful thanks are also extended to the support technicians at the computational chemistry software company SCM. Advice given by Mr. Pier Philipsen, Mr. Mirko Franchini and Mr. Thomas Soini have been of great assistance in offering me the abilities necessary for running their program. A special thanks to Senior Engineer Terje Røsten at the Faculty of Natural Sciences administration at NTNU, for his efforts in setting me up with computational resources. And thanks to the team at the computer software company Plotly, for providing me with the tools for handling the data and producing the graphics. I wish to thank my parents, Nimon and Wenche, for their everlasting encouragement, their help and their faith in me throughout my studies. My friends, Sindre, Benjamin, Schweinhoon and Gayan for their treasured friendship. And finally, and most importantly, I would like to thank my wife Kristine. Her beautiful support, flawless patience and uplifting presence has been paramount to this thesis, and everything else in my life.

# Table of Contents

# List of Tables

# List of Figures

# Abbreviations

| | | |
|---|---|---|
| B88 | = | Becke Exchange Functional |
| BLYP | = | Becke and Lee-Yang-Parr Exchange-Correlation Functional |
| BZ | = | Brillouin Zone |
| CB | = | Conduction Band |
| DFT | = | Density Functional Theory |
| DFTB | = | Density-Functional Tight-Binding |
| DOS | = | Density of States |
| GGA | = | Generalized Gradient Approximation |
| HF | = | Hartree-Fock |
| IB | = | Intermediate Band |
| IBSC | = | Intermediate Band Solar Cell |
| IBZ | = | Irreducible Brillouin Zone |
| LDA | = | Local Density Approximation |
| LYP | = | Lee-Yang-Parr Correlation Functional |
| MO | = | Molecular Orbital |
| PBEc | = | Perdew-Burke-Ernzerhof Correlation Functional |
| PBEx | = | Perdew-Burke-Ernzerhof Exchange Functional |
| PDOS | = | Partial Density of States |
| PW91 | = | Perdew-Wang Exchange-Correlation Functional |
| PW91c | = | Perdew-Wang Correlation Functional |
| PW91x | = | Perdew-Wang Exchange Functional |
| SCF | = | Self-Consistent Field |
| TM | = | Transition Metal |
| VB | = | Valence Band |
| XC | = | Exchange-Correlation |

Chapter 1

# Introduction

Every day vast amounts of solar radiation is incident on earth. Solar cells provide a way of utilizing this radiation to supply the world with clean renewable energy. At present time this technology is of immense importance due the challenges we are faced with in terms of climate change and global warming. Yet, for solar cells to compete in the global energy market they need to have high efficiencies. As the efficiency of solar cells play such a key role, much highly-motivated research is going into ways of increasing its value. One idea which has shown much promise for improving the efficiency has been the formation an intermediate band (IB) inside the band gap of solar cell semiconductors [1]. Solar cells based on this idea are termed intermediate band solar cells (IBSC) and they have been shown to yield theoretical efficiency limits as high as 63.1% [2]. Single bandgap solar cells have a corresponding efficiency limit of 40.7%. One way of realizing materials in possession of such desired intermediate bands is by transition metal doping [3]. Silicon is prevalent in the solar cell industry and insight into its workings as a material is abundant. Hence, the formation of intermediate bands in silicon is highly attractive. Common transition metals possess electronic states belonging to $d$ shells. As such states do not exist for silicon, doping may lead to strong perturbations in its electronic structure, giving rise to intermediate bands [4]. In this thesis the formation of intermediate bands in silicon by transition metal doping is studied by method of density functional theory (DFT) and density-functional tight-binding (DFTB). Firstly, chapter 2 brings the theoretical framework for understanding solar cells, and as an extension, the IBSC concept. This chapter also brings forward important terminology and ideas necessary for performing the calculations, such as concepts related to crystal structure, electronic band structure and the Fermi level. Chapter 3 gives the theoretical framework for density functional theory, which is necessary for understanding our calculations and results. Due to density-functional tight-binding being an approximate DFT method its theoretical framework is not individually discussed in this thesis. However, a brief description of DFTB is to be found in chapter 4. Chapter 4 discusses our methods and brings forward computational details. Chapter 5 is reserved for our results and discussions, before we in chapter 6 draw conclusions and lastly give some suggestions for future work in chapter 7.

Chapter 2

# Theoretical Framework for Solar Cells

In the following, an introduction to the theoretical framework for solar cells will be given. First, the center of attention will be theory on crystalline materials, the Fermi level and electronic band structure. From thereon the focus shifts more generally into the properties of semiconductors and light, before the standard solar cell is familiarized and the idea of an intermediate band solar cell is brought forward. The following chapter is primarily based on reference [5].

## 2.1 Crystal structures

Most solar cell materials are *crystalline*, meaning they can be characterized by their atoms orderly periodic arrangements. Because of this, the entire crystal structure of a material may be described by repeating a small region of the crystal. The smallest region possible to use for reconstructing the locations of all the atoms in a crystal is called the *primitive cell*. But sometimes this primitive cell have a somewhat difficult geometry which may not be well suited for a specific application, then a larger *unit cell* can be used, which has a simpler shape and also contain all the information needed, see figure 2.1a. The unit cell edge length is termed the *lattice constant*.

Typical solar cell materials, such as silicon (Si) crystals, gallium arsenide (GaAs) crystals and cadmium sulfide (CdS) crystals have an atomic arrangement generally called a *diamond lattice*. The unit cell of such a diamond lattice or diamond cubic crystal structure can be viewed in figure 2.1b.

When atoms come together to form a crystal, the electrons in the outer shells are shared with neighboring atoms, hence their energy levels are affected, and new closely spaced sets of energy levels emerge, as opposed to those associated with electrons in an isolated atom. These sets are called *energy bands*. And these bands of energies allowed to electrons may

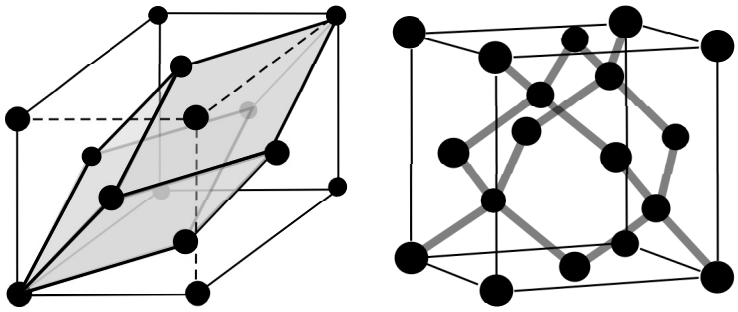


**Figure 2.1:** (a) Fcc unit cell, with the primitive cell shown in grey. (b) Unit cell of the diamond cubic crystal structure.

overlap or be separated by gaps of forbidden energies ($E_g$), depending on the characteristic distances between the atoms in the crystal.

## 2.2 The Fermi level

At temperatures close to absolute zero, electrons in a crystal will occupy the lowest possible energy states. And due to the *Pauli exclusion principle*, each allowed energy state will be filled by, maximum, two electrons, each of opposite spin. As a consequence, all available energy states in the crystal up to a certain level will be occupied by electrons. This energy level is known as the *Fermi level* ($E_F$).

As temperature increases, electrons gain energy and there will be some probability of electrons occupying states above the Fermi level, as well as probabilities of states below the Fermi level being empty. The *Fermi-Dirac distribution function f(E)*, gives the probability of occupation of an allowed electron state of energy E, and it is as follows,

$$f(E) = \frac{1}{1 + e^{(E-E_F)/k_B T}} \tag{2.1}$$

where $k_B$ is Boltzmann's constant and $T$ is the absolute temperature.

The Fermi-Dirac distribution is plotted in figure 2.2. Here it can be seen that for a temperature $T_1$ near absolute zero, the probability of occupation $f(E)$ is essentially unity up to the Fermi level $E_F$. As the temperature increases, as with $T_2$ and $T_3$, the probability of occupation spreads out and gives energy states above the Fermi level finite probability above zero, and energy states below the Fermi level finite probability below unity. Hence possibilities of electrons occupying states above the Fermi level, and states below the Fermi level being empty.

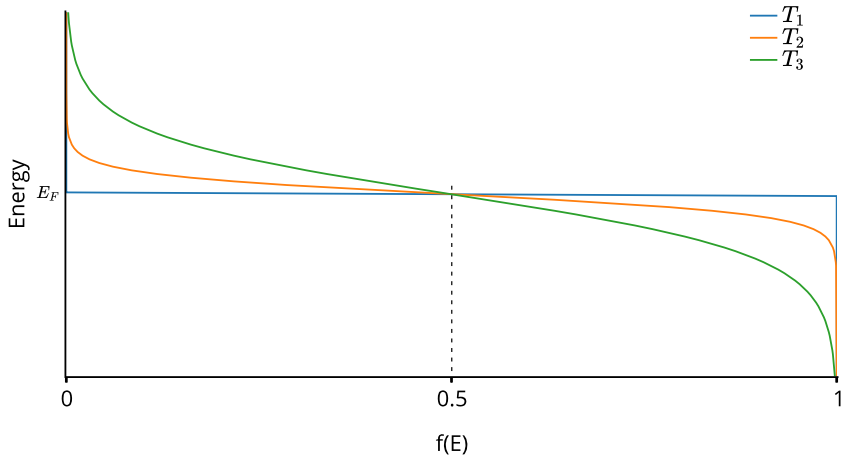


**Figure 2.2:** Fermi-Dirac distribution for temperatures $T_1 \approx 0$ and $T_3 > T_2 > T_1$.

## 2.3 Electronic band structure

Using the Fermi level and what was previously mentioned about crystal structures and energy bands, it is possible to give a distinction between metals, insulators and semiconductors. Metals have an electronic band structure such that the Fermi level lies within an allowed band. Insulators have the Fermi level inside a relatively large energy gap between a band fully occupied by electrons and a next higher band which is empty of electrons (at low temperatures). And semiconductors are similar to insulators only they have the Fermi level inside a relatively narrow band gap. See figure 2.3 for principal sketch of this distinction.

The material used in a solar cell is usually a semiconductor. At low temperatures there is no current flow in the semiconductor crystal, since a completely filled band means no vacant allowed energy levels nearby for electrons to be excited into, and an empty band have no contribution. But for higher temperatures the Fermi-Dirac distribution spreads out and some energy levels are left vacant in the previously completely filled band, termed the *valence band* (VB), and some energy levels are filled in the previously completely empty band, termed the *conduction band* (CB). Now current may flow in the conduction band as electrons have many unoccupied energy states nearby to be excited into, and current may flow in the valence band as vacancies leaves energy states for electrons to be excited into, leaving new vacancies for other electrons to be excited into, and so on. The current in the conduction band is of course described by the motion of the electrons, but the current in the valence band is more easily described by the motion of the single vacant energy states, and these states are often modeled as physical particles of positive charge, commonly termed *holes*.

The motion of electrons and holes in semiconductors differs somewhat from the motion

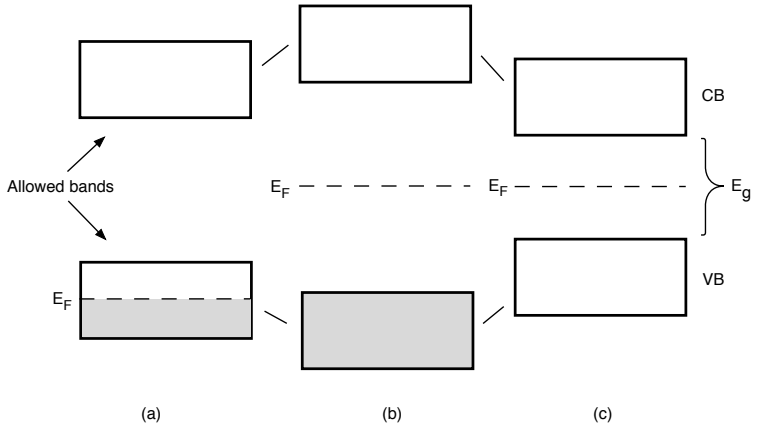


**Figure 2.3:** Distinction between (a) metals, (b) insulators and (c) semiconductors.

of particles in free space. Whereas the energy ($E$) and momentum ($p$) of a free electron of mass ($m$) is related by,

$$E = \frac{p^2}{2m} \tag{2.2}$$

the analog relation for electrons and holes near the conduction band minimum ($E_c$) and the valence band maximum ($E_v$) respectively is,

$$E - E_c = \frac{(p - p_0)^2}{2m_e^*} \tag{2.3}$$

and

$$E_v - E = \frac{(p - p_0')^2}{2m_h^*} \tag{2.4}$$

where $m_e^*$ and $m_h^*$ denotes the effective masses of electron and hole due to the periodic force of the lattice atoms and $p$ is the crystal momentum analogous to the free space momentum of equation 2.2. If $p_0 = p_0'$ the semiconductor is known as a *direct-band-gap semiconductor* and if $p_0 \neq p_0'$ its known as a *indirect-band-gap semiconductor*. GaAs is an example of a direct-band gap semiconductor and Si an example of a indirect-band-gap semiconductor. The two situations are illustrated in figure 2.4.

The actual energy distribution of electrons and holes in the semiconductor may be calculated from density of states and probability of occupation of these states. The details of these calculations will not be gone into here, but results are presented. The number of allowed states per unit volume for energies corresponding to the forbidden band gap is zero. And in the absence of anisotropy the number of allowed states near the conduction band edge can be described by,

$$N(E) = \frac{8\sqrt{2}\pi m_e^{*3/2}}{h^3}(E - E_c)^{1/2} \tag{2.5}$$

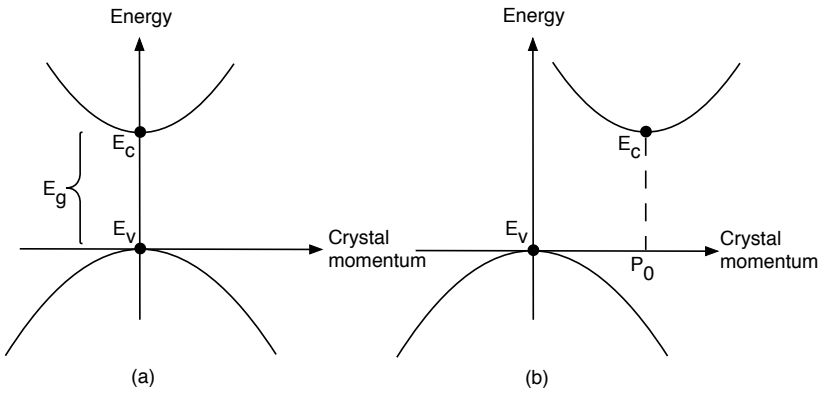


**Figure 2.4:** (a) Direct-band-gap semiconductor. (b) Indirect-band-gap semiconductor.

with a corresponding expression for energies near the valence band edge, here $h$ is Planck's constant. The number of electrons in the conduction band, $n$, per unit volume of the crystal goes as

$$n = N_C e^{(E_F - E_c)/k_B T} \tag{2.6}$$

whilst the number of holes in the valence band, $p$, per unit volume of the crystal goes as

$$p = N_V e^{(E_v - E_F)/k_B T} \tag{2.7}$$

where $N_C$ and $N_V$ are the *effective density of states* in the conduction band and valence band respectively ($N_C$ and $N_V$ are constant at fixed $T$).

## 2.4 Bond model and impurities

Now the effects of impurities in crystalline group IV semiconductors will be discussed in terms of the bonds between atoms in their lattice. More specifically, the focus will be on silicon as it is an important group IV semiconductor in terms of solar cell applications, and it serves well to illustrate the points to be made.

Silicon has four valence electrons and is bonded to four neighboring atoms by covalent bonds. This means that each covalent bond shares one electron from the central Si and one electron from a neighboring Si. At low temperatures the electrons making up the bonds do not have enough energy to break free from the bonds and can not contribute to current flow in the crystal. But at higher temperatures some electrons may obtain enough energy to release themselves from covalent bonds and be free to roam around throughout the crystal, whilst also leaving empty spots behind for electrons in nearby covalent bonds to move into, both contributing to current flow, see figure 2.5. This situation is analogous to the previous discussion on electronic band structure; For an electron to break free from a covalent bond, a minimum of energy equal to the forbidden band gap is required. An electron who breaks free can be seen as in the conduction band. And an empty spot left behind can be viewed as a hole in the valence band.

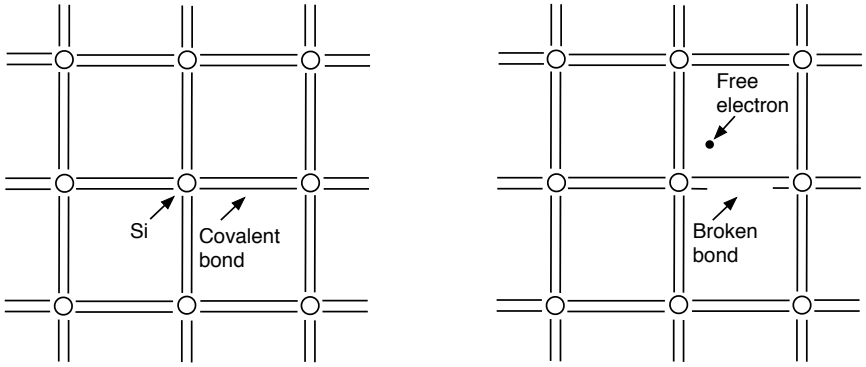


**Figure 2.5:** Bond model of the silicon crystal lattice.

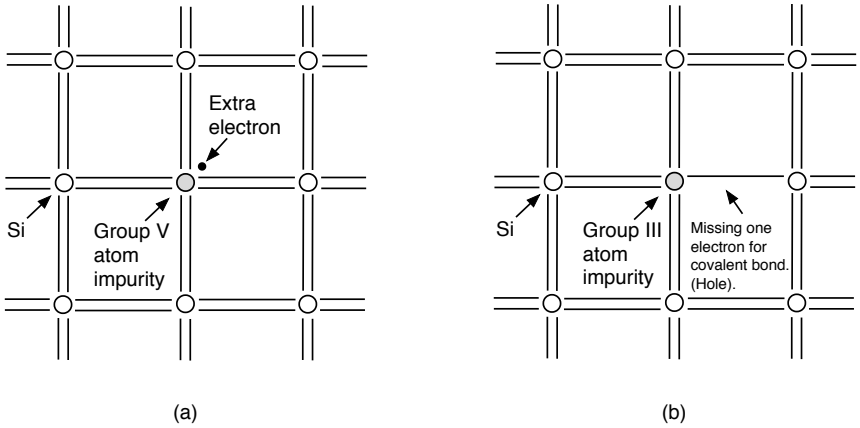


**Figure 2.6:** Bond model of the silicon crystal lattice with (a) donor impurity and (b) acceptor impurity.

Moving on to impurities, particularly *substitutional impurities*, meaning impurities substituting for atoms in the semiconductor, such that the regular crystal structure atomic arrangement is maintained. For silicon it is usually group III and group V atoms which acts as such impurities. With a group V impurity in Si, four of the valence electrons of the impurity will take part in the covalent bonding, whilst the extra electron is in a different situation, neither in the valence band nor the conduction band (see figure 2.6). As can be calculated, the ionization energy $E_i'$ required for the extra electron to be free to move around in the crystal, that is, to be in the conduction band is approximately 0.02 eV, which is much less than the forbidden band gap energy of around 1.1 eV for Si. Hence, the extra electron is at an energy level $E_i'$ just below the conduction band. So in other words this impurity has created an allowed energy level within the so called forbidden band gap. Such a group V impurity is suitably termed a *donor*, and a material with donor impurities is termed *n-type material* (see figure 2.7).

The group III impurities are somewhat analogous, they only have three valence elec-

trons to contribute to the covalent bonding, which leaves a hole (modeled as a physical particle of positive charge) and this hole contributes to an allowed energy level just above the valence band. Such a group III impurity is suitably termed an *acceptor*, and a material with acceptor impurities is termed *p-type material* (see figure 2.6 and 2.7).

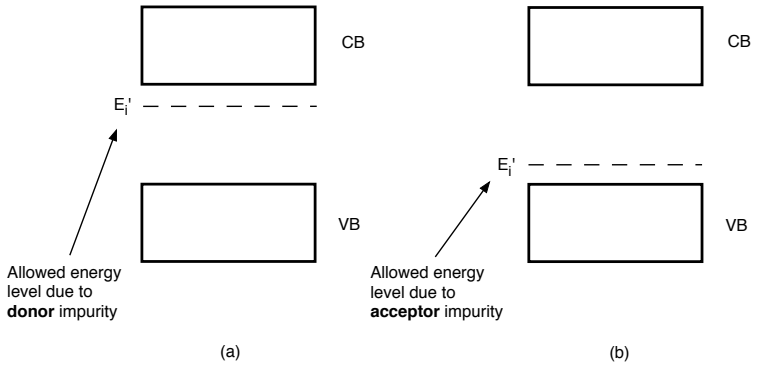


**Figure 2.7:** Introduction of allowed energy levels inside the forbidden gap by (a) donor (b) acceptor.

Lastly, it should also be noted here that the Fermi level of a semiconductor material will shift from a midgap position and move towards the conduction band or valence band according to the concentration of donors and acceptors in the material.

## 2.5 The standard solar cell

The working principle of a standard solar cell is in essence a junction between n-type and p-type material regions, which under illumination can produce a current, enabling power extraction from the cell. Theory around this working principle will now be brought forward.

### 2.5.1 The pn-junction

One of the requirements for there to be an energy conversion from solar energy into electrical energy is that it needs to be an electronic asymmetry in the structure of the semiconductor used. For the case of the standard solar cell this is accomplished by bringing together n-type and p-type semiconductor materials to form a region termed the *pn-junction*. The theory behind this idea lies in the fact that the n-type materials have high electron densities and low hole densities, whereas p-type materials have low electron densities and high hole densities. When brought together, the asymmetry in carrier (electron/holes) transport properties of the two materials creates the needed characteristics for a standard solar cell. As the pn-junction is formed the difference in carrier concentrations leads to the fact that electrons from the n-type material side will move to the p-type material side and holes from the p-type material side will move to the n-type material side. This will not go on forever as the leaving of one side creates charge imbalance. When electrons leave the n-type side it exposes ionized donors of positive charge, whilst the holes leaving the p-type side exposes

ionized acceptors of negative charge. This sets up an electric field opposing the movement of electrons and holes from one side to the other. As the natural diffusion (movement) of electrons and holes keep on going the electric field gets stronger and stronger, and at one point an equilibrium situation will be obtained. Now, a system in thermal equilibrium can only have one Fermi level, but as mentioned earlier, the Fermi level of a semiconductor material shifts according to donor and acceptor impurities. That is, the Fermi level of n-type and p-type materials will lie at different locations in the band gap (see part (a) and (b) of figure 2.8). Now since the pn-junction system can only have one Fermi level the situation needs to be as in part (c) of figure 2.8). Away from the junction conditions may be as in isolated materials, but in the *transition region* from one material to the other there will be a potential change $V_0$. This potential change can be calculated from

$$qV_0 = E_g - E_1 - E_2 \tag{2.8}$$

where $q$ is the electronic charge and $E_1$ and $E_2$ corresponds to energy differences between Fermi levels and valence and conduction bands as in part (c) of figure 2.8. These values can be found by taking equations 2.6 and 2.7 into account to find the locations of Fermi levels in each type of material. For the n-type material with donor impurities the case is as

$$n = N_D = N_C e^{(E_F - E_c)/k_B T} \tag{2.9}$$

where $N_D$ denotes number of electrons in the conduction band per unit volume of the material with donor impurities. Hence for Fermi level it follows

$$E_F - E_c = k_B T \ln\left(\frac{N_D}{N_C}\right). \tag{2.10}$$

Similarly, for the p-type material with acceptor impurities it is found

$$p = N_A = N_V e^{(E_v - E_F)/k_B T} \tag{2.11}$$

where $N_A$ denotes number of holes in the valence band per unit volume of the material with acceptor impurities. And the Fermi level follows as

$$E_v - E_F = k_B T \ln\left(\frac{N_A}{N_V}\right). \tag{2.12}$$

This leads to the following for the potential change,

$$qV_0 = E_g - k_B T \ln\left(\frac{N_V}{N_A}\right) - k_B T \ln\left(\frac{N_C}{N_D}\right). \tag{2.13}$$

And for the idealized case

$$n = p = n_i \tag{2.14}$$

where $n_i$ denotes *intrinsic concentration*, the band gap energy can be found from

$$n_i^2 = np = N_C N_V e^{-E_g/k_B T}. \tag{2.15}$$

And lastly the expression for the potential change is obtained as,

$$V_0 = \frac{k_B T}{q} \ln\left(\frac{N_A N_D}{n_i^2}\right). \tag{2.16}$$

And with an applied voltage, $V_a$, the potential across the transition region becomes $V_0 - V_a$.

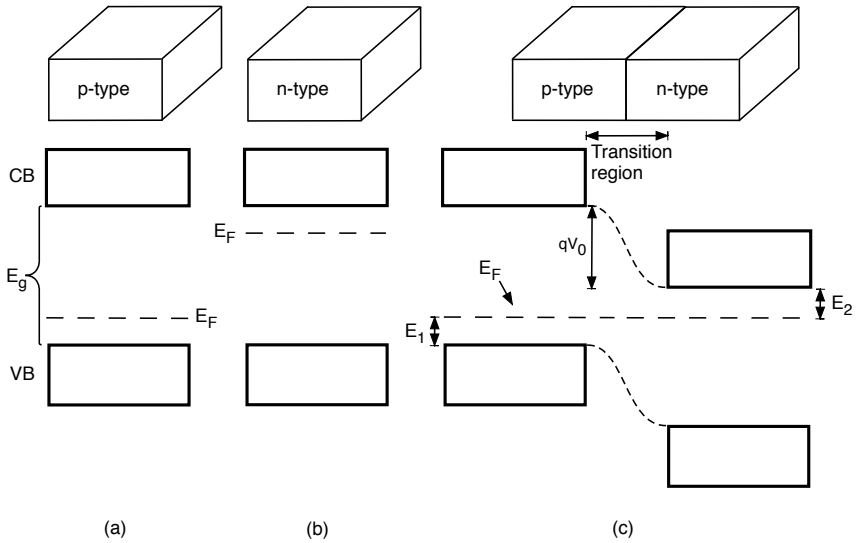


**Figure 2.8:** Schematic representation of the pn-junction.

It will also be instructive here to go into what is called *the depletion approximation*, dividing the system into two regions; *quasi-neutral regions* and *depletion region*. This situation is illustrated in figure 2.9.

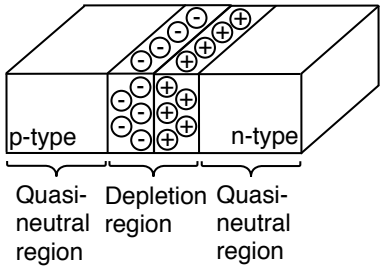


**Figure 2.9:** Schematic representation of the depletion approximation.

The depletion region stems from the diffusion of electrons and holes across the junction and the resulting electric field. This sets up a region depleted of mobile charge carriers, and thereby its name depletion region. In the quasi-neutral regions the space charge density is assumed zero, whilst in the depletion region the space charge density is assumed to have only contributions from the ionized impurities. This approximation sharpens up the space charge density distribution, and allows the width of the depletion region to be described as

$$W = l_p + l_n = \sqrt{\frac{2\epsilon}{q}(V_0 - V_a)\left(\frac{1}{N_A} + \frac{1}{N_D}\right)} \tag{2.17}$$

where $l_p$ and $l_n$ denotes the length of the depletion region in the p and n directions respectively, and $\epsilon$ is the electric constant. The maximum electric field strength in the region can be described by

$$\xi_{\text{max}} = -\sqrt{\frac{2q}{\epsilon}(V_0 - V_a)\Big/\left(\frac{1}{N_A} + \frac{1}{N_D}\right)}. \tag{2.18}$$

Physical characteristics obtainable from the depletion approximation with the region extending equal lengths in p and n directions, can be viewed in figure 2.10.

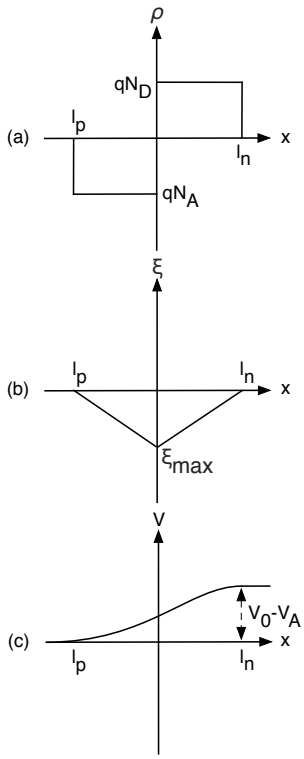


**Figure 2.10:** Depletion approximation characteristics. (a) space charge density distribution (b) electric field distribution (c) potential distribution. All corresponding to one another.

### 2.5.2 Generation and recombination

The concept of generation and recombination of excess charge carriers within semiconductor materials is paramount to the understanding of solar cells. This is where the solar rays

come into play, when light (photons) is incident on a semiconductor it can be absorbed by using up its energy on exciting electrons from their occupied low-energy states into higher unoccupied energy states. This may generate electron-hole pairs, but these pairs may also recombine in various ways.

### Reflection and transmission

Only the light which is transmitted into the semiconductor can be absorbed, some light will be reflected, and the fraction of light reflected for normal incidence can be expressed as

$$R = \frac{(\hat{n}-1)^2 + \hat{k}^2}{(\hat{n}+1)^2 + \hat{k}^2} \tag{2.19}$$

where $\hat{n}$ and $\hat{k}$ comes from the complex *index of refraction*, $\hat{n}_c = \hat{n} - i\hat{k}$ of the absorbing material, $\hat{k}$ is specifically termed the *extinction coefficient*. For silicon about 30% of light of all wavelengths of interest in solar cell work is reflected. This is not good for the efficiency, so antireflection coatings and other strategies is usually employed for reducing that number.

The rate of absorption of the light which is actually transmitted into the semiconductor is proportional to the flux of photons (intensity) for a given wavelength. This leads to a decay in intensity of light ($\mathscr{I}$) as it passes through the semiconductor, and for monochromatic light this can be described as

$$\mathscr{I} = \mathscr{I}(x_0)e^{-\alpha(x-x_0)} \tag{2.20}$$

where $\alpha$ is a function of wavelength known as the *absorption coefficient*, and $x$ moves in the direction of further into the semiconductor. The absorption coefficient is especially of interest in regards of solar cell design as it gives an indication of how far below the surface of a solar cell a particular wavelength of light will be absorbed. The absorption coefficient and extinction coefficient is related by

$$\alpha = \frac{4\pi f \hat{k}}{c} \tag{2.21}$$

where $f$ is the frequency of a plane wave of light, and $c$ is the speed of light in vacuum.

Light of suitable wavelength will generate electron-hole pairs within a semiconductor. The annihilation or absorption of a photon by the excitation of an electron from valence band into conduction band whilst also leaving a hole in the valence band, is termed *fundamental absorption*. This may take place in various ways, and typically the process will be different for indirect-band-gap semiconductors and direct-band-gap semiconductors. This is due to the fact that; Energy and momentum must be conserved, and photons typically have relatively large energy $E_{\text{photon}} = hf$ and small momentum $h/\lambda$. Whilst direct-band-gap semiconductors have band edges at the same value of crystal momentum, indirect-band-gap semiconductors have band edges at different values of crystal momentum.

### Direct-band-gap absorption

Since photon momentum is relatively small compared to the crystal momentum, for a direct-band-gap semiconductor the energy difference for an interband transition is essentially just equal to the energy of the absorbed photon,

$$E_f - E_i = E_{\text{photon}} \tag{2.22}$$

where $E_f$ and $E_i$ denotes the energy of the final and initial electron state respectively. Hence the minimum photon energy required for an interband transition is given by the forbidden band gap,

$$E_{\text{photon}_{\text{min}}} = E_g. \tag{2.23}$$

As photon energy increases, the transitional crystal momentum location will shift further away from the band edge. Away from the band edge the density of electrons at initial state energies increases as well as the density of empty states at final state energies. This increases the probability of absorption and consequently the absorption coefficient is increasing with increasing photon energies above $E_g$.

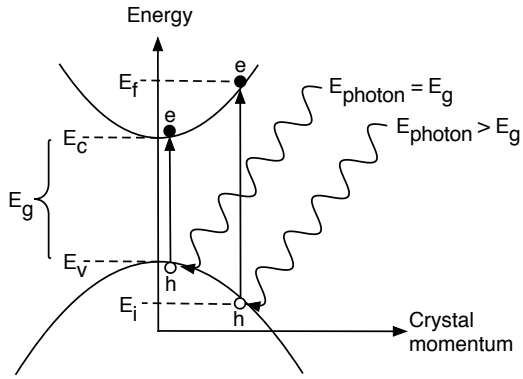


**Figure 2.11:** Schematic illustration of direct-band-gap absorption

### Indirect-band-gap absorption

For indirect-band-gap semiconductors the valence band maximum and conduction band minimum lie at different values of crystal momentum, hence photon energies much larger than the band gap, $E_g$, is required to give a *direct* interband transition. Yet, *indirect* transitions are possible at lower energies, by means of a *phonon*, which can be thought of as a particle corresponding to the coordinated vibration of the atoms making up the semiconductor crystal. Since phonons have relatively small energies and large momentum compared to photons, they particularly contribute needed momentum for a transition to be achievable by lower energy photons. These transitions are made possible both by phonon

absorption and emission (see figure 2.12). Therefore, the minimum photon energy required for exciting an electron from valence band into conduction band can be described by

$$E_{\text{photon}} = E_g - E_{\text{phonon}} \tag{2.24}$$

where $E_{\text{phonon}}$ particularly denotes the energy of a phonon with the specific momentum required for the transition. The probability of absorption is less for the indirect-band-gap case then for the direct-band-gap case, as the indirect-band-gap case involves the added phonon. Consequently the absorption coefficient is also lower, and light may pass further into the semiconductor before being absorbed.

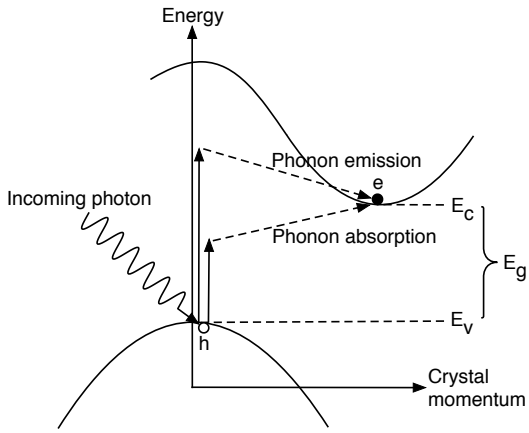


**Figure 2.12:** Schematic illustration of direct-band-gap absorption

It should be noted that direct transitions may also occur in indirect-band-gap semiconductors as long as photons of high enough energy is absorbed. Likewise, indirect transitions may occur in direct-band-gap semiconductors if phonons contribute. And in general there can also be absorption of photons exciting electrons to higher energy states within a band itself, where phonon absorption and emission also may play a role. Furthermore, absorption of light is also possible between bands and energy levels introduced by impurity atoms, such as the levels previously discussed, that is, transitions between bands and the energy levels illustrated in figure 2.7.

### Recombination

As light shines on a semiconductor, appropriate wavelength photons will generate electron-hole pairs. Hence the charge carrier concentrations will be higher for an illuminated semiconductor relative to one in the dark. If the light is switched off such that a previously illuminated semiconductor finds itself in the dark, then the charge carrier concentrations will decay back to equilibrium values, this process is known as *recombination*. In the following, three recombination processes are brought forward. It should be noted that these may take place in parallel, and that for such a case the total recombination rate is simply given by the sum of each rate. Also, *carrier lifetimes* can be defined for each process by

$$\tau_e = \frac{\Delta n}{U} \tag{2.25}$$

$$\tau_h = \frac{\Delta p}{U} \tag{2.26}$$

for electrons and holes respectively. Here $\Delta n$ and $\Delta p$ are the disturbances from equilibrium values $n_0$ and $p_0$ of respective carriers, and $U$ is net recombination rate.

- **Radiative recombination**. This is simply the reverse of the absorption processes previously described. Electrons occupying higher energy states relative to their thermal equilibrium states, may make transitions into empty lower energy states by emitting photons of appropriate energy. Carrier lifetimes for this process is typically smaller for direct-band-gap materials such as GaAs, relative to indirect-band-gap materials such as Si.
- **Auger recombination**. This recombination process is different from the radiative one in the respect that instead of emitting a photon to make a transition into a lower energy state, the excess energy is given to a second electron which then will emit a photon to relax back. The second electron may be in the conduction band or the valence band (only the conduction band case is shown in figure 2.13b). This process is especially effective in relatively highly doped materials, and is the dominant recombination process for good quality Si with impurity concentrations greater than $10^{17}$ cm$^{-3}$.
- **Recombination through traps**. This process relies on energy levels inside the forbidden gap provided by impurities and defects in semiconductors. Electrons may relax down from conduction band energies into valence band energies stepwise via the energy levels (called *trapping levels*) inside the forbidden gap, ultimately recombining with a hole. This process is especially effective for impurities introducing energy levels near midgap. And, also at the surfaces of semiconductor materials this process is very effective, due to the multiple energy levels introduced into the forbidden gap by many surface defects.

### 2.5.3 Efficiency

To discuss the efficiency of the standard solar cell, it is first necessary to familiarize the parameters; *short-circuit current* ($I_{sc}$), *open-circuit voltage* ($V_{oc}$) and *fill factor* (FF). These are all parameters characterizing the operation and performance of a typical pn-junction solar cell. A simplified description of the solar cell operation can be given as follows: Sunlight on the cell generates electron-hole pairs, these are separated by the asymmetrical electronic structure of the cell (the electric field of the depletion region), this separation and the potential difference across the pn-junction give rise to current flow in a load which is connected between cell terminals.
Terminal properties can be viewed in figure 2.14, it shows the short-circuit current as the current of the cell when the voltage is zero, that is, at that point equal to the light-generated

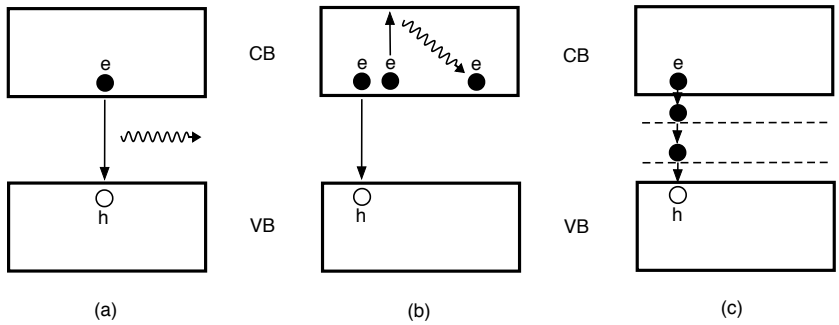


**Figure 2.13:** Schematic illustration of (a) radiative recombination (b) auger recombination (c) recombination through traps.

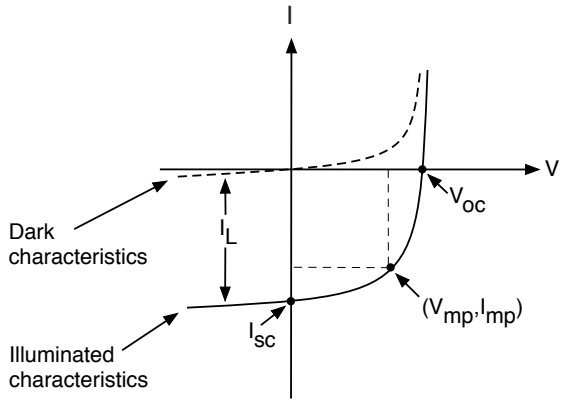


**Figure 2.14:** Terminal properties of pn-junction solar cell.

current ($I_{\mathrm{L}}$). It also shows the open-circuit voltage, that is, the voltage at which there is zero current at the terminals. The fill factor is defined as

$$\mathrm{FF} = \frac{V_{\mathrm{mp}} I_{\mathrm{mp}}}{V_{\mathrm{oc}} I_{\mathrm{sc}}} \tag{2.27}$$

where $V_{\mathrm{mp}}$ and $I_{\mathrm{mp}}$ are the voltage and current at the operating point p which maximizes the power output (see figure 2.14). Hence, the fill factor gives the ratio of the maximum power output relative to a power given by $V_{\mathrm{oc}} \cdot I_{\mathrm{sc}}$. An energy-conversion efficiency, $\eta$, can now be given as

$$\eta = \frac{V_{\mathrm{mp}} I_{\mathrm{mp}}}{P_{\mathrm{L}}} = \frac{V_{\mathrm{oc}} I_{\mathrm{sc}} \mathrm{FF}}{P_{\mathrm{L}}} \tag{2.28}$$

where $P_{\mathrm{L}}$ is the total power of the light incident on the cell.

The energy-conversion efficiency of a solar cell is immensely important, and of course the higher the efficiency the better. There are various ways of calculating an upper limit to

the efficiency, the specifics of these calculations will not be brought forward here, instead some of the factors at play are discussed and an efficiency upper limit is simply given.

Firstly, there will be an upper limit to the obtainable short-circuit current. This is due to the fact that not all incident photons will give rise to electron-hole pairs, in ideal efficiency calculations the assumption is usually taken that each photon with energy greater than the band gap leads to one electron flowing in the external circuit. So to find the maximum short-circuit current the incident photon flux is investigated and this is typically done for AM0, AM1.5, or 6000 K blackbody radiation. The 6000 K blackbody radiation approach is modelling the solar spectrum from its surface temperature, AM0 stands for *air mass zero*, and is modelling the radiation power (per unit area perpendicular to the direction of the sun) outside earth's atmosphere at mean earth-sun distance, and AM1.5 is typically the terrestrial standard. For different solar cells, the ones with smaller band gaps give higher maximum short-circuit currents, as more photons will have the energy required to give electrons flowing in the circuit.

For the open-circuit voltage the situation is reversed, decreasing band gap give lower maximum open-circuit voltage. Obtaining an upper limit to the open-circuit voltage has a basis in the following equations; The open-circuit voltage for an ideal pn-junction cell described as

$$V_{\text{oc}} = \frac{k_B T}{q} \ln\left(\frac{I_L}{I_0} + 1\right) \tag{2.29}$$

with $I_0$ denoting the pn-junction diode saturation current, which can be given as

$$I_0 = A\left(\frac{qD_e n_i^2}{L_e N_A} + \frac{qD_h n_i^2}{L_h N_D}\right) \tag{2.30}$$

where $A$ is cross-sectional area, $D_e$ and $D_h$ are diffusion coefficients, and $L_e$ and $L_h$ are diffusion lengths for electrons and holes respectively. From equation 2.29 one finds that a minimum $I_0$ gives a maximum $V_{\text{oc}}$, from there the parameters in equation 2.30 can be varied within values required for useful solar cells, that is, in order to obtain a minimum $I_0$ and an upper limit to the open-circuit voltage. The band gap dependency of the upper limit can be found from the strong dependency of $I_0$ on the intrinsic concentration $n_i$ which in turn depends on the band gap. The maximum of the fill factor in terms of the energy-conversion efficiency need not be examined separately as it turns out that its maximum will be a function of the open-circuit voltage, whose ideal limit now has been discussed.

With the reverse effect of band gap size on $V_{\text{oc}}$ relative to $I_{\text{sc}}$, estimates of optimum band gaps for the energy-conversion efficiency can be made. For the pn-junction cell these optimum band gaps are typically in the range of 1.4 to 1.6 eV. With upper limit of the energy-conversion efficiency being found to be around 26% for AM0 and 29% for AM1.5. One major efficiency loss mechanism is thermalisation, the fact that electrons and holes relax back to band edges (by emitting phonons) after absorption of photons of greater than band gap energies. Also a major loss mechanism is the fact that even though carriers are separated by a potential corresponding to the band gap, the voltage output can only be a fraction of this potential. Also noteworthy is the fact that efficiency decreases with increasing temperature, that there are losses due to cell reflection, that some light might

pass right through the cell and that electrical contacts will block some of the light. And also recombination will of course have a negative effect on the efficiency.

There are as stated previously many ways of calculating an upper limiting efficiency to the solar cell. Not going into the specifics of the calculations, there have been research indicating a theoretical so called Shockley-Queisser limiting efficiency of as high as 41% for a single gap solar cell [1]. This was under the assumption of isotropic sunlight illumination with a concentration of 46 050 suns (full concentration). Under the assumption of 1 sun illumination a maximum efficiency has been found to be 31% [6]. And a GaAs solar cell has demonstrated that there is possible to approach these kinds of efficiencies, as it showed an efficiency of 28.8% [2]. For solar cells other than the standard pn-junction one, higher theoretical efficiency limits are proposed, particularly the *intermediate band solar cell* (IBSC) has an upper limiting efficiency as high as 63% under full concentration [2].

## 2.6 The intermediate band solar cell

This section is based upon references [2, 7, 8, 9].

The intermediate band solar cell and its high theoretical efficiency limit relies on the usage of a semiconductor with an extra set of energy levels inside the band gap, a so called intermediate band (IB), and in this context such a semiconductor material is termed an IB-material. This IB-material is placed between two regular p- and n-type semiconductors which acts as selective contacts to valence band and conduction band respectively.

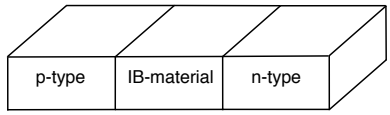


**Figure 2.15:** Illustration of the p-IB-n structure of the IBSC

With the IB-material sub-band gap absorption is possible, that is, photon absorption processes from both VB to IB and IB to CB, in addition to the usual VB to CB (see figure 2.16). This is due to the partially filled IB, with both empty states that electrons from the VB can be excited into, and filled states with electrons that can be excited into the CB. These two sub-band gap transitions are depicted as 1 and 2 respectively in figure 2.16, together with the transition from VB to CB depicted as 3.

The sub-band gap absorption processes yields higher utilization of photons incident on the IBSC. With this configuration photons of less than band gap energies can create electron-hole pairs, via the two steps VB-IB and IB-CB. Hence, the photocurrent obtainable in the IBSC is higher than that of the standard pn-junction solar cell. This does not immediately lead to a higher efficiency solar cell, as not only the photocurrent is responsible for the efficiency, but also the voltage. For investigating the voltage, the standard solar cell is briefly considered again as a reference. Under illumination the pn-junction solar cell is not in thermal equilibrium, however thermal equilibrium can exist independently within the hole population of the VB and the electron population of the CB. Thus, the carrier populations may be considered as in quasi-thermal equilibrium, and electron and

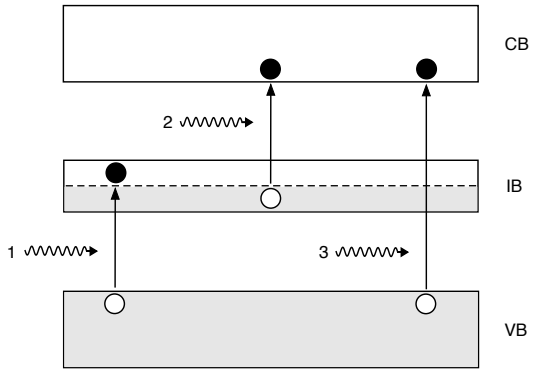


**Figure 2.16:** Schematic of absorption processes and transitions for the IBSC.

hole distributions may be described independently by *quasi-Fermi levels* (QFLs). The energy difference between these QFLs, that is, the corresponding electrochemical potential difference, $\mu_1$, give rise to the voltage of the solar cell. Now with the IBSC there will be a third population of carriers, the electrons and holes in the IB, which will be in its own quasi-thermal equilibrium and thereby will be describable by a third QFL. These three QFLs sets up three different electrochemical potential differences $\mu_{1,2,3}$ with the relation $\mu_1 = \mu_2 + \mu_3$ (see figure 2.17).

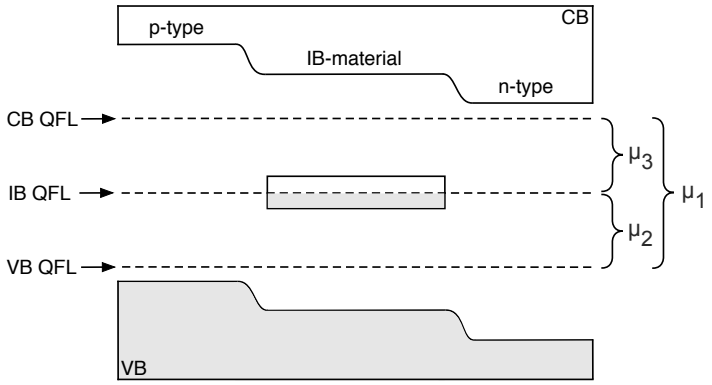


**Figure 2.17:** Schematic of the p-IB-n structure with QFLs and electrochemical potential differences.

Yet, with the IB-material located between the p- and n-type semiconductors acting as selective contacts to VB and CB respectively, there is no electrical contact to the IB. Hence it is $\mu_1$ which again give rise to the voltage of the solar cell, that is, the IBSC voltage corresponds to that of the standard solar cell, and thereby the increased photocurrent yields higher efficiency. There exist multiple approaches to how one may realize IBSCs, however, this thesis is focused on the approach of transition metal doping of bulk materials. Looking to see if impurity atoms may modify the electronic band structure such that intermediate

bands will have formed.

Chapter 3

# Theoretical Framework for DFT Calculations

In the following, an introduction to the theoretical framework for DFT calculations will be given. It will not investigate all the theoretical aspects that DFT calculations touches upon, but it will bring forward the main ideas relevant for the scope of this thesis. A primary reference for this chapter is reference [10].

## 3.1 The Schrödinger equation

Density functional theory deals with finding solutions to the fundamental equation that describes the quatum behavior of atoms and molecules, the Schrödinger eqaution [11]. It applies the Born-Oppenheimer approximation, which separates the atoms nuclei and electrons into two seperate mathematical problems, due to their difference in mass [12]. And it is interested in the time-independent, nonrelastivistic Schrödinger equation, where multiple electrons are interacting with multiple nuclei [10]:

$$\left[ -\frac{\hbar}{2m} \sum_{i=1}^{N} \nabla_i^2 + \sum_{i=1}^{N} V(\mathbf{r}_i) + \sum_{i=1}^{N} \sum_{j<i} U(\mathbf{r}_i, \mathbf{r}_j) \right] \psi = E\psi. \tag{3.1}$$

Here, $\hbar$ is the reduced Planck constant, $m$ the electron mass, $V(\mathbf{r}_i)$ the potential defined by the interaction between an electron at position $\mathbf{r}_i$ and the collection of atomic nuclei, $U(\mathbf{r}_i, \mathbf{r}_j)$ the potential due to the interaction between an electron at position $\mathbf{r}_i$ and another at position $\mathbf{r}_j$, $\psi$ is the electronic wave function and $E$ is the ground state energy of the electrons. Hence, the three terms in the brackets of equation (3.1) are determining, for each electron, the kinetic energy, the interaction energy with the nuclei, and the interaction energy with different electrons. Solving this equation and extracting from its solutions the properties for a collection of atoms, is not as straightforward as one might think. The

electronic wave function is a function of each of the three spatial coordinates of each of the $N$ electrons:

$$\psi = \psi(\mathbf{r}_i, \dots, \mathbf{r}_N). \tag{3.2}$$

This means that if we were to try and solve the Schrödinger equation for, let's say, a single Silicon atom, it yields a full wave function of 42 dimensions. Furthermore, a cluster of only a 100 Silver atoms would result in a full wave function requiring a staggering 14100 dimensions. Needless to say, it gets ugly in a hurry.

## 3.2 Hartree-Fock (HF) method

In order to deal with the complexity of the full electronic wave function, one strategy is to approximate the function as a product of individual electron wave functions:

$$\psi = \chi_1(\mathbf{x}_1)\chi_2(\mathbf{x}_2), \dots, \chi_N(\mathbf{x}_N). \tag{3.3}$$

This is known as the Hartree product [13]. And the individual electron wave functions $\chi$ are called *spin orbitals*. Spin orbitals have both spin and spatial components, and these components are defined by the $\mathbf{x}$ vector.

The Hartree product can be attractive from a numerical point of view, but it fails to describe nature in a satisfactory way, as it does not fulfill the Pauli exclusion principle, a fundamental principle of quantum physics [14]. A wave mechanical formulation of the Pauli exclusion principle, for electrons, can be given as [15]:

> *For electrons, there is an exclusion of all classes of states different from the antisymmetrical one.*

That is, in terms of a mathematical formulation, an interchange of any two electron coordinates demands a change of sign in the wave function:

$$\psi(\mathbf{r}_1, \mathbf{r}_2, \dots, \mathbf{r}_N) = -\psi(\mathbf{r}_2, \mathbf{r}_1, \dots, \mathbf{r}_N) \tag{3.4}$$

Clearly, this is not true for the Hartree product, and quickly, this product approximation gave way for the Hartree-Fock (HF) method [16]. The HF method approximates the full electronic wave function by using a product that is entirely antisymmetric, the Slater determinant [17]:

$$\psi = \frac{1}{\sqrt{N!}} \begin{vmatrix} \chi_1(\mathbf{x}_1) & \chi_2(\mathbf{x}_1) & \cdots & \chi_N(\mathbf{x}_1) \\ \chi_1(\mathbf{x}_2) & \chi_2(\mathbf{x}_2) & \cdots & \chi_N(\mathbf{x}_2) \\ \vdots & \vdots & \ddots & \vdots \\ \chi_1(\mathbf{x}_N) & \chi_2(\mathbf{x}_N) & \cdots & \chi_N(\mathbf{x}_N) \end{vmatrix}. \tag{3.5}$$

This approximation fulfills the Pauli exclusion principle, and thereby contains physical information leading to a more accurate description of nature. Similar to the Hartree product, this approximation also decouples the electrons into single-electron wave functions (spin

orbitals). And consequently the Schrödinger equation (3.1) is transformed into a set of single-electron Schrödinger equations of the following form [10, 18]:

$$\left[-\frac{\hbar}{2m}\nabla^2 + V(\mathbf{r}) + V_H(\mathbf{r}) - \mathcal{K}\right]\chi_j(\mathbf{x}) = E_j\chi_j(\mathbf{x}). \tag{3.6}$$

By comparing this equation (3.6) with the Schrödinger equation in (3.1), it becomes clear that the summation signs are gone and the electron-electron interaction term is replaced by a *Hartree* potential, $V_H$, and an *exchange* term $\mathcal{K}$. The Hartree potential is defined as:

$$V_H = e^2 \int \frac{n(\mathbf{r}')}{|\mathbf{r} - \mathbf{r}'|}\,\mathrm{d}^3r' \tag{3.7}$$

and this potential is due to the decoupling of electrons, as one assumes that electrons are moving independently of each other. Meaning, the electrons are not effected by instantaneous forces between them, but by Coulomb repulsion averaged over all electron positions. It is this Coulomb repulsion that is brought forward by the Hartree potential in equation (3.7), where $e$ is the electron charge and $n$ is the electron density. Moving on to the exchange term $\mathcal{K}$, this term is a consequence of the antisymmetrical description of the wave function (the Slater determinant), and its name originates from its feature of exchanging spin orbital indices. A further discussion on the mathematical definition of the exchange term will not be given here, as it is not seen as needed, for the level of introduction to DFT being delivered.

Now, to solve the single-electron Schrödinger equation numerically, one needs to approximate the spin orbitals from a finite set of functions, as one cannot describe an arbitrary continuous function on a computer. This approximation of spin orbitals can be written as [10]:

$$\chi_j(\mathbf{x}) = \sum_{i=1}^{K} \alpha_{j,i}\phi_i(\mathbf{x}) \tag{3.8}$$

where $\alpha$ represents the expansion coefficients, and $\phi$ constitutes the finite set of functions (called *basis set*) being used for approximating the spin orbitals. Due to the circular approach of the HF method, the Schrödinger equation must be solved in an iterative way, making an initial guess for the spin orbitals and repeating the calculations until the spin orbitals reproduce themselves within a reasonable limit. This limit is often called the *convergence* criteria, and when the limit is reached, the calculations are said to be *converged*. This iterative way of solving the Schrödinger equation is called a *self-consistent field* (SCF) method, as it looks to see if the functions from the solutions are consistent with the functions producing the solutions, i.e. looking to see if they are self-consistent.

Lastly, the term *correlation* energy should be mentioned. Since the HF method is an approximation, it yields energy results different from the exact energy of the systems investigated. This difference between the energy result obtained by the HF method and the exact energy of the system, is called correlation energy [19]:

$$E_{\text{correlation}} = E_{\text{exact}} - E_{\text{HF}}. \tag{3.9}$$

It has its name from the approximation of electrons as only interacting through an average potential, $V_H$, that is to say; the electrons are uncorrelated. Hence adding the correlation energy to a HF energy solution would represent *correlating* the electrons. In other words, the HF method fails to represent electron correlation; it ignores the fact that electrons are correlated, and "avoid" each other more than an average potential suggests. This failure can generate energy solutions that are too low, and lead to HF predictions that are clearly wrong [20]. Together with its, sometimes wrong property predictions, the HF method can also be viewed as too time-consuming for systems with large number of atoms. Henceforth, it is time to turn away from Hartree-Fock, and over to an approach more suitably quick and accurate, that is, density functional theory (DFT), the approach most frequently used for large numerical calculations in solids [21].

Before moving onward though, it should be noted: That the motivation behind the introduction of the terminology that has been used in this section, such as; *exchange*, *correlation*, *basis set*, *self-consistent field* and *convergence*, is on the basis of these terms being especially relevant for density functional theory. As the terms are frequently used to describe elements and aspects of the DFT calculations.

## 3.3 Density functional theory (DFT)

Density functional theory is a most popular tool for the investigation of matter, and it has opened up unexpected horizons in the understanding and predicting capability of matters electronic and structural properties [22]. The success of DFT, and its attribute as being the first choice for approaching large numerical calculations in solids, is largely based on its use of the electron density as the basic variable. By using the electron density, instead of the wave function, the dimensionality of the problems posed are greatly reduced. Regardless of how many electrons a system consists of, the electron density remains 3 dimensional, and issues disappear, such as those discussed earlier concerning Silicon and Silver, and their need for 42 and 14100 dimensions.

### 3.3.1 Thomas-Fermi (TF) model

Without going into details, the idea of using only the electron density to determine electronic energy was first incorporated in the 1920s by Thomas and Fermi [23, 24]. The kinetic energy of a systems electrons was then derived from quantum statistical theory based on the uniform electron gas, whilst the rest was treated classically, resulting in the following expression for the total energy [25]:

$$E[n] = \frac{3}{10}\left(2\pi^2\right)^{2/3} \int n^{5/3}(\mathbf{r})\mathrm{d}\mathbf{r} - Z\int \frac{n(\mathbf{r})}{r}\mathrm{d}\mathbf{r} + \frac{1}{2}\int\int \frac{n(\mathbf{r}_1)n(\mathbf{r}_2)}{|\mathbf{r}_1 - \mathbf{r}_2|}\mathrm{d}\mathbf{r}_1\mathrm{d}\mathbf{r}_2. \quad (3.10)$$

Here, this equation will only serve as an illustration of the fact that total energy may be expressed in terms of the electron density exclusively. The TF model is only a preliminary to present-day DFT. And next, the foundations on which current DFT calculations rests will be presented.

### 3.3.2 The Hohenberg-Kohn theorems

Density Functional Theory rests upon two mathematical theorems, these are the Hohenberg-Kohn theorems [26]:

> **Theorem 1:** *The ground-state energy from Schrödinger's equation is a unique functional of the electron density.*
>
> **Theorem 2:** *The electron density that minimizes the energy of the overall functional is the true electron density corresponding to the full solution of the Schrödinger equation.*

Simplified, the first theorem states that the ground state wave function is one-to-one with the ground-state electron density. And the second theorem gives a method for finding the ground-state electron density. That method being a *variational principle*, varying the electron density until the energy of the functional is minimized. Here, a functional is a function of a function, and the functional described by the Hohenberg-Kohn theorems is the key to finding the solution to the Schrödinger equation. This functional is an energy functional, and a useful mathematical description for this functional was developed by Kohn and Sham [27]. The relationship between the functional and the Schrödinger equation, goes via the electron density, and as previously stated, in DFT the electron density is the basic variable, so the discussion should start there.

### 3.3.3 Kohn-Sham equations

Density functional theory derives the true electron density from a single Slater determinant, and the orbitals that define this determinant, are the so called *Kohn-Sham orbitals* [28]. These orbitals are defined by [10, 29]:

$$n(\mathbf{r}) = 2\sum_i \psi_i^*(\mathbf{r})\psi_i(\mathbf{r}) \tag{3.11}$$

where, $n$ is the electron density at a particular position, $\mathbf{r}$, in space, and $\psi$ are the Kohn-Sham orbitals. These orbitals were originally purely mathematical constructions for the purpose of obtaing the electron density, but one can now say that there is essential physics in these orbitals; that they can be termed molecular orbitals (MO), and that they can be thought of as individual electron wave functions, whereas the factor of 2, above in their defining equation, is due to the Pauli exclusion principle [10, 30, 31]. Although equation (3.11) is the defining equation for the orbitals, the equation itself only gives the electron density by "using" these orbitals, the orbitals themselves have to be found from the *Kohn-Sham equation* [28]. This equation is the DFT counterpart to the Schrödinger equation considered in the HF method. And arriving at this Kohn-Sham equation (Schrödinger equation), Kohn and Sham defined a mathematical form for the energy functional described by Hohenberg-Kohn theorems, this energy functional can be written as [10, 27]:

$$E[\{\psi_i\}] = E_{\text{known}}[\{\psi_i\}] + E_{\text{XC}}[\{\psi_i\}]. \tag{3.12}$$

Here, $E_{\text{known}}$ represents the terms that can be written down in a simple analytical form, and $E_{\text{XC}}$ represents all the quantum mechanical effects not included in $E_{\text{known}}$. Where, $E_{\text{XC}}$

is termed the *exchange-correlation functional* (XC-functional). And $E_{\text{known}}$ includes four contributions [32]:

$$\begin{aligned} E_{\text{known}}[\{\psi_i\}] = &-\frac{\hbar^2}{m}\sum_i \int \psi_i^* \nabla^2 \psi_i \,\mathrm{d}^3 r + \int V(\mathbf{r}) n(\mathbf{r}) \,\mathrm{d}^3 r \\ &+ \frac{e^2}{2}\int\int \frac{n(\mathbf{r}) n(\mathbf{r}')}{|\mathbf{r}-\mathbf{r}'|} \,\mathrm{d}^3 r \,\mathrm{d}^3 r' + \sum_I \sum_{J\neq I} \frac{Z_I Z_J}{|\mathbf{R}_I - \mathbf{R}_J|} \end{aligned} \tag{3.13}$$

which are, in order, the electron kinetic energies, Coulomb interactions between electron and nuclei, Coulomb interactions between pairs of electrons, and Coulomb interactions between pairs of nuclei. The true exact general form of the exchange-correlation functional, $E_{\text{XC}}$, on the other hand, is not yet known. But, there is a whole range of approximations for the exchange-correlation functional, some of which will be examined later in this chapter.

Now that the prerequisites for the Kohn-Sham equation (Schrödinger equation) have been given, the equation can reveal itself in the following way [10, 27]:

$$\left[-\frac{\hbar^2}{2m}\nabla^2 + V(\mathbf{r}) + V_H(\mathbf{r}) + V_{\text{XC}}(\mathbf{r})\right]\psi_i(\mathbf{r}) = \epsilon_i \psi_i(\mathbf{r}). \tag{3.14}$$

Here, many similarities to the Hartree-Fock equation (3.6) can be found, as it is roughly of the same form, only here the exchange term $\mathcal{K}$, is replaced by an exchange-correlation potential, $V_{\text{XC}}$, which is accounting for effects that Hartree-Fock fails to account for. Also, the Kohn-Sham equation only depend on the three spatial variables from $\psi_i(\mathbf{r})$, and $\epsilon_i$ represents the energies of these single-electron orbitals. One of the unphysical effects that the HF method give rise to, is a Coulomb interaction between an electron and itself, invoked by $V_H$, this self-interaction is corrected by the exchange-correlation potential, and the potential is also meant to contain all quantum mechanical effects not already accounted for. Its definition is formally a "functional derivative" of the exchange-correlation energy functional:

$$V_{\text{XC}}(\mathbf{r}) = \frac{\delta E_{\text{XC}}[n]}{\delta n(\mathbf{r})}. \tag{3.15}$$

Here, $\delta$ represents that this is not a normal derivative, but that conceptually it may be thought of that way.

In order to arrive at a solution, this whole system needs to be solved iteratively, that is by a SCF method. The procedure can be outlined in the following way:

**I** Make initial guess of electron density, $n(\mathbf{r})$.

**II** Use this electron density to solve the Kohn-Sham equation for the Kohn-Sham orbitals, $\psi_i(\mathbf{r})$.

**III** Use these orbitals to define a new electron density, $n_{\text{KS}}(\mathbf{r}) = 2\sum_i \psi_i^*(\mathbf{r})\psi_i(\mathbf{r})$.

**IV** Repeat until convergence is achieved, i.e. $|n_{\text{KS}}(\mathbf{r}) - n(\mathbf{r})| < \text{cc}$, where $n(\mathbf{r})$ is the electron density used to solve the Kohn-Sham equation, $n_{\text{KS}}(\mathbf{r})$ is the electron density resulting from that solution, and cc is a suitably chosen convergence criteria.

Finally, when this iterative method have led to a self-consistent solution, the total energy may be calculated from [33]:

$$E = \sum_{i=1}^{N} \epsilon_i - \frac{1}{2} \int \int \frac{n(\mathbf{r}) n(\mathbf{r}')}{|\mathbf{r} - \mathbf{r}'|} + E_{\mathrm{XC}}[n] - \int V_{\mathrm{XC}}(\mathbf{r}) n(\mathbf{r}) \mathrm{d}\mathbf{r}. \tag{3.16}$$

## 3.4 The exchange-correlation functional

The Kohn-Sham strategy would yield the exact energy, were it not for the fact that the true exchange-correlation functional remains unknown. The approximations begin where the choice of exchange-correlation functional is done. Hence, one might say that the success or failure of a DFT calculation rests on the selection of the functional. A whole range of approximations for the exchange-correlation functional exists, but only two classes of approximations will be presented here, based on their enhanced relevance for this thesis; *The local density approximation* (LDA), and *the generalized gradient approximation* (GGA).

### 3.4.1 The local density approximation (LDA)

Although the true form of the exchange-correlation functional is unknown, its form for the special case of a uniform electron gas can be derived exactly. The local density approximation makes use of this fact by dividing real inhomogenous systems into infinitesimal volumes, where each volume contains an electron density considered as constant. The exchange-correlation energy of each volume is then approximated as that of the uniform electron gas at that density. And furthermore the total exchange-correlation energy of the system can then be obtained by [25]:

$$E_{\mathrm{XC}}^{\mathrm{LDA}}[n] = \int n(\mathbf{r}) \epsilon_{\mathrm{XC}}(n(\mathbf{r})) \mathrm{d}\mathbf{r} \tag{3.17}$$

where $\epsilon_{\mathrm{XC}}$ is the exchange-correlation energy per particle of the interacting uniform electron gas of density $n(\mathbf{r})$. Here $\epsilon_{\mathrm{XC}}$ is usually divided into separate exchange, $\epsilon_{\mathrm{X}}$, and correlation, $\epsilon_{\mathrm{C}}$, terms, where $\epsilon_{\mathrm{X}}$ can be obtained analytically by the method of Bloch or Dirac, and $\epsilon_{\mathrm{C}}$ may be obtained from parametrization of quantum Monte Carlo [1] simulations of the uniform electron gas [34, 35, 36].

This approximation may seem of little practical value, since real materials have variations in electron density, and these variations often are what makes the materials interesting. But, although this approximation do not consider variations/gradients, it has shown good useful results, even for highly inhomogeneous systems [37]. Solids have especially been successfully investigated using LDA, where experimental lattice parameters for example, have been reproduced within only a few percent [38]. And in solid-state physics LDA have been applied to calculations of total energies and band structures for many years. The success of LDA, in spite of ignoring gradients, partly comes from systematic

[1] quantum Monte Carlo is a time-consuming highly accurate computational technique providing essentially exact answers to quantum mechanical equations

error cancellations between overestimates of exchange energies and underestimates of correlation energies [39]. But, of course, LDA have some issues and may be improved on, and this is where the generalized gradient approximation comes into play.

### 3.4.2 The generalized gradient approximation (GGA)

As the LDA uses information about the local electron density, the generalized gradient approximation adds information about the local gradient in the electron density. This additional information is incorporated as to improve on the approximation of the exchange-correlation functional, and hence is meant to yield better DFT calculation results (at the cost of higher computational effort and time). The use of GGA as a substitute for LDA, do not necessarily always mean more accurate calculations, and better results, as there are multiple ways of incorporating the gradient into the approximation, that is, there exists multiple GGAs, and hence multiple outcomes can be found. But for many properties, such as, geometries and ground state energies of molecules and solids, GGAs can be found superior, and said to yield better results. Schematically, this approximation can be written as [40]:

$$E_{\mathrm{XC}}^{\mathrm{GGA}}[n] = \int f^{\mathrm{GGA}}(n(\mathbf{r}), \boldsymbol{\nabla} n(\mathbf{r}))\mathrm{d}\mathbf{r} \tag{3.18}$$

where, $f^{\mathrm{GGA}}$ refers to some function of both electron density and its gradient. Here this will be taken a bit further, and some particular GGA exchange-correlation functionals will be brought forward, since GGAs consists of some of the most widely used functionals in DFT [41].

In GGA, the exchange and correlation parts are modeled separately, whereas:

$$E_{\mathrm{XC}}^{\mathrm{GGA}} = E_{\mathrm{X}}^{\mathrm{GGA}} + E_{\mathrm{C}}^{\mathrm{GGA}}. \tag{3.19}$$

and $E_{\mathrm{X}}^{\mathrm{GGA}}$ takes the form:

$$E_{\mathrm{X}}^{\mathrm{GGA}}[n] = \int n(\mathbf{r})\epsilon_{\mathrm{X}}^{\mathrm{LDA}}(n(\mathbf{r}))F_{\mathrm{X}}^{\mathrm{GGA}}(s)\mathrm{d}\mathbf{r} \tag{3.20}$$

whilst $E_{\mathrm{C}}^{\mathrm{GGA}}$ can consist of several different complicated analytical forms, hence can not be presented in this way here [42]. In the exchange part, $\epsilon_{\mathrm{X}}^{\mathrm{LDA}}(n(\mathbf{r}))$ corresponds to that of the LDA, formerly mentioned in the above section, and $F_{\mathrm{X}}^{\mathrm{GGA}}(s)$ is an enhancement factor, enhancing the exchange energy value of the LDA for a given electron density $n$ at position $\mathbf{r}$, and it does so by incorporating the electron density. Where the argument $s$ of the enhancement factor is a dimensionless variable consisting of both the electron density and its gradient, that is, a reduced dimensionless density gradient defined as [43]:

$$s = \frac{|\boldsymbol{\nabla} n(\mathbf{r})|}{(24\pi^2)^{1/3} n(\mathbf{r})^{4/3}}. \tag{3.21}$$

Now presenting, some of the most widely used exchange functionals, as they differ only in the $F_{\mathrm{X}}^{\mathrm{GGA}}$ term. Also, some analytical representations for different popular correlation functionals will be brought forward here. These representations serve only as to give an

idea of how these functionals look, their level of mathematical sophistication and to help fixate their variations to something else than just their names. No explicit explanation to the nature of the parameters involved in the expressions will be given here, due to the reasoning behind their introduction in the first place, but their mathematical definitions can be found in the appendix if this should be of interest. The functionals brought forward are the popular, Becke (B88) exchange functional, the Perdew-Wang (PW91) exchange and correlation functionals, the Perdew-Burke-Ernzerhof (PBE) exchange and correlation functionals, and the Lee-Yang-Parr (LYP) correlation functional[2].

Becke (B88) uses enhancement factor [45]:

$$F_{\mathrm{X}}^{\mathrm{B88}}(s) = \frac{1 + s \cdot a_1 \cdot \sinh^{-1}(s \cdot a_2) + a_3 \cdot s^2}{1 + s \cdot a_1 \cdot \sinh^{-1}(s \cdot a_2)}, \tag{3.22}$$

Perdew-Wang (PW91x) uses enhancement factor [46]:

$$F_{\mathrm{X}}^{\mathrm{PW91}}(s) = \frac{1 + s \cdot a_1 \cdot \sinh^{-1}(s \cdot a_2) + \left(a_3 - a_4 \cdot e^{-100s^2}\right)s^2}{1 + s \cdot a_1 \cdot \sinh^{-1}(s \cdot a_2) + a_5 \cdot s^4}, \tag{3.23}$$

and Perdew-Burke-Ernzerhof (PBEx) uses enhancement factor [47]:

$$F_{\mathrm{X}}^{\mathrm{PBE}}(s) = 1 + a_6 - \frac{a_6}{\left(1 + \frac{a_7}{a_6}s^2\right)}. \tag{3.24}$$

Perdew-Burke-Ernzerhof correlation functional (PBEc) can be written as [47]:

$$E_{\mathrm{C}}^{\mathrm{PBE}} = \int n(\mathbf{r})\left(\epsilon_{\mathrm{C}}^{\mathrm{LDA:PW}} + g^3\frac{\beta^2}{2\alpha}\ln\left[1 + \frac{2\alpha}{\beta}\frac{t^2 + At^4}{1 + At^2 + A^2t^4}\right]\right)\mathrm{d}\mathbf{r},$$

Perdew-Wang correlation functional (PW91c) as [48]:

$$\begin{aligned} E_{\mathrm{C}}^{\mathrm{PW91}} = \int n(\mathbf{r})\Bigg(&\epsilon_{\mathrm{C}}^{\mathrm{LDA:PW}} + g^3\frac{\beta^2}{2\alpha'}\ln\left[1 + \frac{2\alpha'}{\beta}\frac{t^2 + A't^4}{1 + A't^2 + A'^2t^4}\right] \\ &+ \left(\frac{16}{\pi}\right)\left(3\pi^2\right)^{1/3}\left[C_c(r_s) - C_c(0) - \frac{3C_x}{7}\right]g^3t^2\exp\left[-100g^4t^2\left(\frac{k_s^2}{k_F^2}\right)\right]\Bigg)\mathrm{d}\mathbf{r}, \end{aligned}$$

and lastly, the Lee-Yang-Parr correlation functional (LYP) can be written as [49]:

$$\begin{aligned} E_{\mathrm{C}}^{\mathrm{LYP}} = -a\int \frac{1}{1 + d n(\mathbf{r})^{-1/3}}\Bigg[&\mathbf{r} + bn(\mathbf{r})^{-2/3}\Bigg(C_F n(\mathbf{r})^{5/3} \\ &- 2t_w + \left(\frac{1}{9}t_w + \frac{1}{18}\nabla^2 n(\mathbf{r})\right)e^{-cr^{-1/3}}\Bigg)\Bigg]\mathrm{d}\mathbf{r} \end{aligned}$$

[2]The presented analytical representations for B88, PW91, PBE and LYP, being given here, are loosely based on the representations which may be found in references [40], [43] and [44].

DFT calculations can use different combinations of exchange and correlation functionals, and these combinations have their own names, for example, B88 and LYP is called BLYP, and PW91x and PW91c is simply called PW91. These functionals satisfy some of the known conditions that the true exact exchange-correlation functional must satisfy, and they yield better binding and atomic energies than the local density approximation. They are widely used and often produce usable results. As mentioned earlier, there exist other classes of functionals as well, these can be even more sophisticated and take into account even more information, and satisfy more conditions. Some are called meta-GGAs, and hyper-GGAs, but they often come at the cost of very high computational effort, and will thereby not be of interest for this thesis.

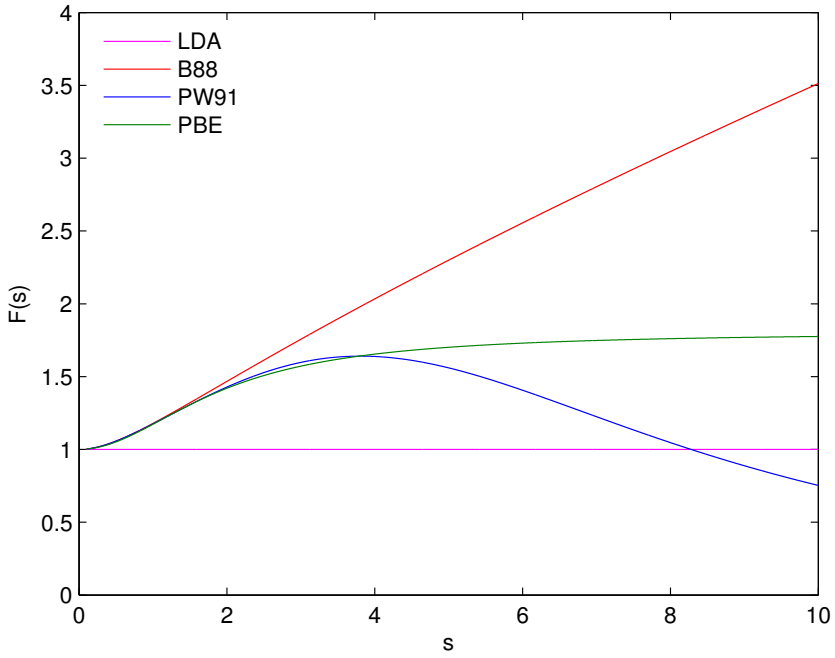


**Figure 3.1:** Enhancement factors of the GGA exchange functionals of B88, PW91 and PBE, together with the LDA.

## 3.5 Bloch's theorem and k-space

The DFT calculations of interest to this thesis are the ones which are applied to bulk crystalline materials. As mentioned in a previous chapter, crystalline materials have their atoms in periodic arrangements, which makes it possible to describe the entire crystal by repeating cells of appropriate geometry with atoms suitably placed within. In the framework of DFT the name *supercell* is used as the term for the vectors defining this cell volume and

placement of atoms. The placements, or rather the positions of the atoms can be given by using normal three-dimensional Cartesian coordinates and defining lattice vectors. In this way positions $\mathbf{r}$ can be given as

$$\mathbf{r} = n_1\mathbf{a}_1 + n_2\mathbf{a}_2 + n_3\mathbf{a}_3 \tag{3.25}$$

where $n_{1,2,3}$ are integers and $\mathbf{a}_{1,2,3}$ are the lattice vectors. For cubic crystal structures the lattice vectors are orthogonal and of equal length. This length is typically termed the *lattice constant* and is denoted simply by the letter $a$.

With the periodic arrangements of atoms there will be a periodic potential and Bloch's theorem states that in the presence of a periodic potential the solutions to the Schrödinger equation can be given as a sum of terms with the following form

$$\phi_{\mathbf{k}}(\mathbf{r}) = u_{\mathbf{k}}(\mathbf{r})e^{i\mathbf{k}\cdot\mathbf{r}} \tag{3.26}$$

where

$$u_{\mathbf{k}}(\mathbf{r}) = u_{\mathbf{k}}(\mathbf{r} + n_1\mathbf{a_1} + n_2\mathbf{a_2} + n_3\mathbf{a_3}), \text{ for all } n. \tag{3.27}$$

Meaning $u_{\mathbf{k}}(\mathbf{r})$ is a function of same periodicity as the supercell. The result of Bloch's theorem is thereby a possibility of solving the Schrödinger equation for each wave vector $\mathbf{k}$ independently. The space of the wave vectors $\mathbf{k}$ is called k-space (or reciprocal space), and the lattice vectors of k-space is related to those of real space as follows

$$\mathbf{b}_1 = 2\pi\frac{\mathbf{a}_2 \times \mathbf{a}_3}{\mathbf{a}_1 \cdot (\mathbf{a}_2 \times \mathbf{a}_3)}, \qquad \mathbf{b}_2 = 2\pi\frac{\mathbf{a_3} \times \mathbf{a}_1}{\mathbf{a}_2 \cdot (\mathbf{a}_3 \times \mathbf{a}_1)}, \qquad \mathbf{b}_3 = 2\pi\frac{\mathbf{a}_1 \times \mathbf{a}_2}{\mathbf{a}_3 \cdot (\mathbf{a}_1 \times \mathbf{a}_3)}. \tag{3.28}$$

Making $\mathbf{a}_i \cdot \mathbf{b}_j = 2\pi$ for $i = j$ and $\mathbf{a}_i \cdot \mathbf{b}_j = 0$ for $i \neq j$. It also follows that for cubic crystal structures with lattice constant $|\mathbf{a}_i| = a$, the corresponding length in k-space will be $|\mathbf{b}_i| = 2\pi/a$ for all $i$, and in general longer real space lattice vectors yields shorter lattice vectors in k-space.

Solving the Schrödinger equation for each wave vector $\mathbf{k}$ independently will in part consist of evaluating integrals in k-space. Due to the symmetry of the crystal this need only be done for a specific region in k-space termed the *Brillouin zone* (BZ). This region in k-space has many special properties which will not be gone into detail about here, other than pointing out that its a cell in k-space sufficient for representing the whole crystal structure, and it corresponds to a special kind of primitive cell in real space by the name of Wigner-Seitz cell. By symmetry operations it is not even necessary to evaluate integrals over the entire BZ, but only in a reduced region termed the *irreducible Brillouin zone* (IBZ). By evaluations of the electronic wave functions for each wave vector $\mathbf{k}$ one finds energy bands, now as was shown in section 2.3 energy bands where given in correspondence to crystal momentum, and with the wave vector related to crystal momentum by $\mathbf{k} = \mathbf{p}/\hbar$ the energy bands are equivalently given for $\mathbf{k}$ [50]. Different points and directions in k-space which are highly symmetrical are given special labels, the point where $\mathbf{k} = 0$ is always labeled the $\Gamma$ point. Figure 3.2 shows the IBZ of an fcc lattice with labelling of high symmetry points and directions, this also corresponds to the IBZ for all diamond and zinc-blende materials e.g. such as Si and GaAs [51, 52].

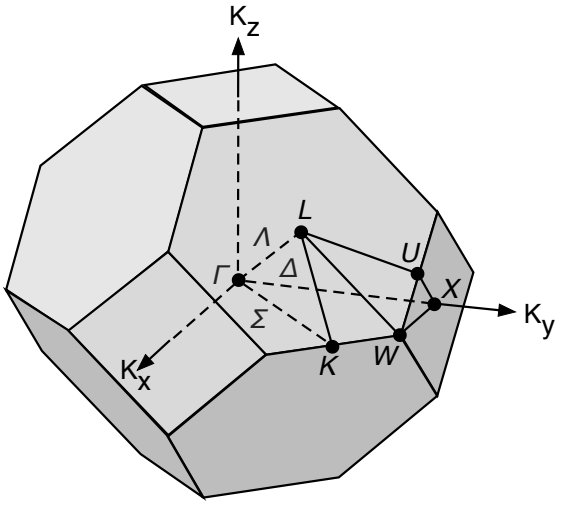


**Figure 3.2:** IBZ of fcc lattice with labelling of high-symmetry directions and points.

Chapter 4

# Method

## 4.1 BAND

Electronic properties are studied by method of DFT. Calculations are performed within the BAND modeling suite of the Amsterdam Density Functional (ADF) program. The ADF Band-structure program (BAND) employs DFT in the Kohn-Sham approach, and is specifically designed for usage on periodic systems, such as crystals. BAND makes use of atomic orbitals, and available basis functions are Slater-Type Orbitals (STOs) and/or Numerical Orbitals (NOs). The STOs are of the form

$$f(\mathbf{r}) = Y_{lm}\mathbf{r}^n e^{-\zeta r}, \tag{4.1}$$

where the basis function center is at a nucleus, $Y_{lm}$ are spherical harmonics, and zeta ($\zeta$) determines the long range decay of the function. The ADF database consist of basis sets of ranging quality, from single-zeta to higher quality quadruple-zeta with various diffuse and polarization functions. The basis set employed in the calculations of this thesis is the triple zeta with two polarization functions (TZ2P).

BAND operates several technical aspects of a calculation by a single key denoted "Numerical Quality", its range is; Basic - Normal - Good - Very Good - Excellent. The key influences the accuracy of the calculation and sets the quality of what is called the Becke grid, Zlm Fit, k-space integration and Soft Confinement. The Becke Grid is a numerical integration grid, a refined version of a so called fuzzy cells integration scheme developed by Becke. Zlm Fit is the density fitting scheme, in essence it splits the total electron density into atomic densities which are then approximated by radial spline functions and real spherical harmonics (Zlm). The k-space integration is by default set to use a regular grid and different settings yield different number of points along a lattice vector. The Soft Confinement sets the confinement for all atoms, that is, it alters the radial part of the basis functions making them more compact. With the "Numerical Quality" key set to "Good" all of the above mentioned technical aspect qualities are also set to "Good". To show the meaning of this, the k-space integration is a suitable example. In a 0-5 bohr interval, thinking in real space lattice vectors, the number of points used will be 13 if the setting is set to

”Good”, whereas a ”Basic” setting would only use 5 points. The ”Numerical Quality” of the calculations of this thesis is set to ”Good”.

For speeding up the periodic DFT calculations BAND has the option of using a ”Frozen Core”. This means that inner electrons of atoms are frozen in such a way that the cores are frozen to their optimized atomic configuration. The ”Frozen Core” option can be set to ”Large”, ”Medium” or ”Small”, with the names reflecting the size of the core kept frozen. In the calculations of this thesis the ”Frozen Core” is set to ”Small”. BAND also employs space group symmetry to reduce computational effort in the integrals over the Brillouin Zone.

The exchange-correlation functional chosen for our calculations is the Perdew-Wang (PW91) within the generalized gradient approximation. The calculations are geometry optimizations, meaning calculations are performed and solutions are found self-consistently so as to reach a minimum energy geometry. The convergence criteria used are all defaults within the BAND program, they are set as follows: Energy changes 0.001 Hartree, nuclear gradients 0.001 Hartree/Angstom, bond lengths 0.01 Angstrom, bond- and dihedral angle changes 0.5 degree.

The calculations performed are in the aim of finding suitable IB-materials for the IBSC concept. The search of this project work is in essence a study of the changes in electronic properties of Si by the introduction of different impurities into the crystal lattice. For comparison to impurity concentrations from experimental doping the super cell size requirements are of magnitudes strongly influencing the computational effort and time of the calculations. Due to the time limitation of this thesis, the super cell size of our DFT calculations are not exceeding the 2x2x2 super cell. This poses constraints in the possibility of comparison to experimental results and also constraints when it comes to minimizing the interaction between impurity atoms. However, the calculations will give some first indications on how the impurities will modify the electronic properties of Si. More information about BAND can be found from Ref. [53], which has been a primary reference for the above.

## 4.2 DFTB

The Density-Functional based Tight-Binding (DFTB) modeling suite of the ADF program is used as a pre-optimizer for the periodic DFT calculations with BAND. And it is also used as a method for investigating electronic structures by itself. Information on the modeling suite can be found from Ref. [54]. We here give a very brief description of the method with special regards to DFT:

The DFTB method can be seen as an approximate DFT method allowing investigations of larger systems at a much lower computational cost. The principal idea behind this method is describing the Hamiltonian eigenstates with an atomic-like basis set and replacing the Hamiltonian with a parametrized matrix consisting of elements only depending on internuclear distances and orbital symmetries. The parametrized Hamiltonian matrix as well as overlap matrices are calculated using atom-like valence orbitals derived from DFT. Although the parametrization is coming directly from DFT, absolute transferability to DFT can not be achieved as the starting point for DFTB is in fact as its name suggests *tightly bound* electrons, that is, electron interactions are being treated perturbatively. The

exchange-correlation analog in DFTB is a repulsive potential containing the physics which is problematic and is approximated by using simple functions. It is termed repulsive due to its containment of the ion-ion repulsive interaction, however it also contains other interactions. The fitting of the repulsive potential is done with respect to DFT structures, and in practice this is done by minimizing the force difference $\left|\mathbf{F}^{\mathrm{DFT}} - \mathbf{F}^{\mathrm{DFTB}}\right|$ (where forces are zero for optimized structures). Lastly, we note that reproducing DFTB calculations is typically harder than reproducing DFT calculations. This is due to the fact that DFT calculations have well documented XC-functionals, whereas the case is not so for either the DFTB repulsive functions or the DFTB fitting procedures. For more information about the DFTB method we refer to Ref. [55, 56], which is from where this brief description has arisen.

The DFTB calculations performed in this thesis has employed the *mio-0-1 + hyb-0-2* parameter set for which documentation can be found from Ref. [57]. A *Fermi* fill strategy for the orbitals was used, performing electronic charge distribution over the orbitals using a Fermi temperature specified to 5 K.

## 4.3 Computational details

We look at transition metal doping of bulk Si with a particular focus on Ag as the dopant. The choice of Si is rooted in its typical usage in present-day solar cells, and the existing comprehensive insight into its workings as a solar cell material. This insight might give advantages leading to greater proficiency in the work towards manufacturing actual highly-efficient IBSCs at later stages. The particular focus on Ag as impurity atom in bulk Si is due to the theoretical work by Sullivan et al. in Ref. [9], which points toward Ag being a promising candidate for IB-material development. Furthermore, the IBSC research team at NTNU have readily made samples with Ag in Si.

The computations performed in this thesis are all geometry optimizations, whereas some also optimize the lattice. We investigate bulk Si in cubic crystal diamond structure. The doping of bulk Si is substitutional, that is, Si atoms are substituted at their lattice sites by dopant atoms. The case for Ag-doping of Si at 6.25% impurity concentration is shown in figure 4.1. One Si-atom in the 2x2x2 supercell have been substituted by an Ag-atom, hence the Ag atom is one of the 16 atoms in the supercell, giving impurity concentration of $1/16 = 6.25\%$.

The valence electron configurations of the elements considered, Si, Ag, V, Cr, Mn, Fe, Co are $3s^2 3p^2$, $5s^1 4d^{10}$, $4s^2 3d^3$, $4s^1 3d^5$, $4s^2 3d^6$, $4s^2 3d^7$ respectively.

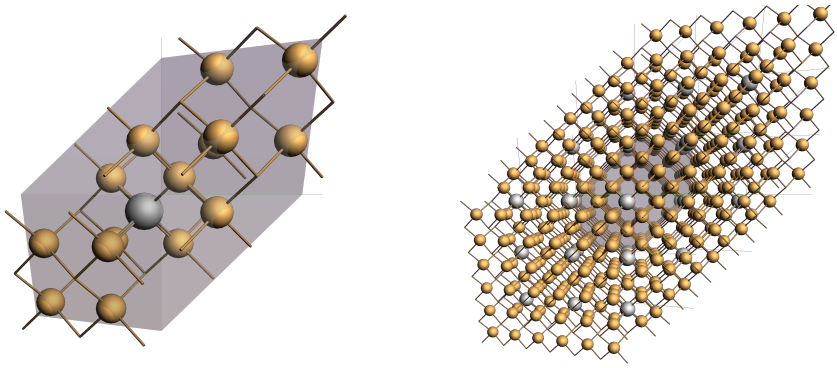

**(a)** 2x2x2 supercell. **(b)** Periodic view.

**Figure 4.1:** Substitutional doping in 2x2x2 supercell. Ag atom depicted in grey.

Chapter 5

# Results and Discussion

Firstly, results from calculations on silicon and silver are presented individually. These are of importance not just in themselves, but also for providing a platform for comparison of our results to those of others, helping us understand the accuracy of our calculations. Afterwards, we move onward to the case of Ag-doped Si. And lastly we bring forward the results from doping by our elected $3d$ series V, Cr, Mn, Fe and Co.

## 5.1 Structural and electronic properties of Si

**Table 5.1:** LDA and GGA calculated band gap of bulk Si, keeping the lattice constant equal to its experimental value $a = 5.43$ Å. Experimental (expt.) band gap is also presented[a]

| | LDA | GGA:PW91 | expt. |
|---|---|---|---|
| $E_g$ (eV) | 0.53 | 0.65 | 1.17 |

[a]Both lattice constant and band gap experimental values were found in Ref. [58].

The calculated band gap of Si from our calculations are presented in table 5.1. Both LDA and GGA calculations correctly display the existence of a band gap in Si, as it is a semiconductor. However the band gap is heavily underestimated in both cases, with the errors of 55% and 44% for LDA and GGA respectively. The reason behind the underestimate of the band gap is ultimately grounded in the fact that the exact exchange-correlation functional remains unknown and both LDA and GGA are as their names suggests, *approximations*.

The underestimate of the band gap is typical for DFT calculations using LDA- and GGA XC-functionals, as is mentioned by Xiao et al. in Ref. [59]. They propose the usage of hybrid functionals including exact Hartree-Fock exchange for better prediction of band

gaps, and demonstrates that the hybrid functional B3PW91 predicts gaps to great precision. The usage of such functionals was not suitable for the purpose of this thesis mainly due to the time scope of the project and the computational cost of hybrid functionals. From Okada et al. in Ref. [2], further methods are brought forward for correcting DFT band gap predictions, and amongst those the application of simple scissor operators expanding the band gap without affecting the band structure, is specifically proposed as a possibility for Si. No specific measures were taken to correct for the band gaps of our calculations, which is to some extent rooted in the objective of this thesis being only to give some first ideas about modifications in electronic properties within Si by substitutional impurities, and look for intermediate band formation. However, that is not to say that band gap corrections could not have been implemented with importance to our results. The importance of the band gap results from our calculations lies in the fact that an IBSC relies on IB-material of appropriate band gap and proper positioning of the IB. And with the underestimation of band gap by DFT also the positioning of energy levels within the gap introduced by impurity atoms can be questionable.

**Table 5.2:** Calculated equilibrium lattice constant of Si by LDA and GGA, together with experimental value.

| | LDA | GGA:PW91 | expt. |
|---|---|---|---|
| $a$ (Å) | 5.41 | 5.47 | 5.43 |

Calculated equilibrium lattice constant of bulk Si is presented in table 5.2. The LDA yields an under-estimate of the lattice constant, giving a theoretical value about 0.4% smaller than the experimental value. The GGA however over-estimates the lattice constant by giving a value 0.7% larger than experimental value. These errors are fairly small and these theoretical results can be said to be somewhat precise. The over-binding character of LDA is well-known, as well as the over-corrections by GGA producing longer bond lengths [58].

The calculated electronic band structure of Si obtained at the GGA:PW91 equilibrium lattice constant ($a = 5.47$ Å) is presented in figure 5.1. The band structure shows the nature of Si as being an indirect band gap material, with the valence band maximum (at $E_v = -5.91$ eV) and conduction band minimum (at $E_c = -5.29$ eV) occurring at different k-points, and with the Fermi level (at $E_F = -5.62$ eV) placed inside the gap. From the figure it is evident that the valence band maximum is found to occur at the zone center ($\Gamma$-point), whereas the conduction band minimum is occurring close to the $X$-point along the $\Delta$ high symmetry direction. The location of the top of the valence band is known from experiment to be at the zone center [60]. And the bottom of the conduction band is known to be located close to the $X$-point in the $\Delta$ direction [61]. Hence these locations are correctly predicted by our calculation, that is without looking to exact k-point values and error estimates.

Energy gaps at the high symmetry points ($\Gamma$, $X$ and $L$) are given in table 5.3 together with the calculated band gap, corresponding experimental values and calculated results from other work. This table 5.3 demonstrates that the results from our calculations are not atypical and that the limitations of DFT at predicting energy gaps is once again evident.

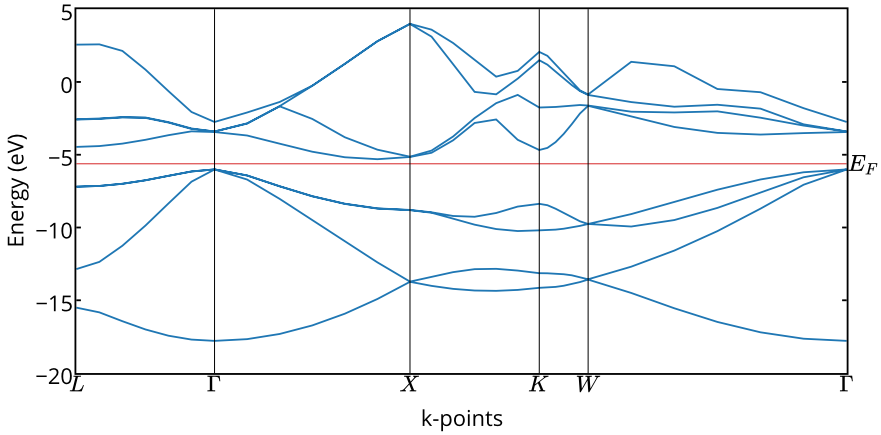


**Figure 5.1:** Calculated band structure of Si, obtained at the GGA:PW91 equilibrium lattice constant.

**Table 5.3:** Calculated energy gaps of Si at selected high symmetry points, together with band gap, corresponding experimental values and GGA:PBE calculated results from other work (calc.)[a]. All values are in eV.

| | GGA:PW91 | calc. | expt. |
|---|---|---|---|
| $E_g$ | 0.62 | 0.61 | 1.17 |
| $\Gamma$ | 2.57 | 2.57 | 3.34 |
| $X$ | 3.64 | 3.56 | 1.25 |
| $L$ | 2.74 | 2.64 | 2.4 |

[a]Experimental values and GGA:PBE calculated results was found in Ref. [58].

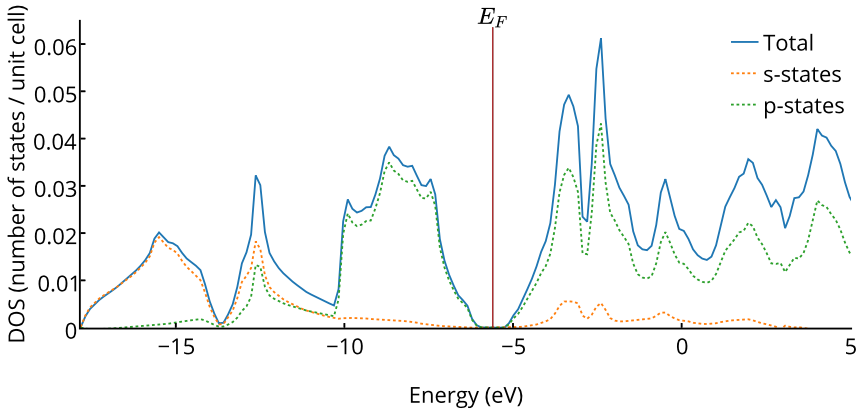


**Figure 5.2:** Calculated density of states with $s$ and $p$ state contributions for bulk Si obtained at the GGA:PW91 equilibrium lattice constant.

The calculated electronic density states for bulk Si obtained at the GGA:PW91 equilibrium lattice constant is presented in figure 5.2. It displays the separation of valence- and conduction band, with the Fermi level inside the band gap, as was displayed by the band structure also. With figure 5.2 showing Si total density of states as well as the contributions from $s$ states and $p$ states, it is possible to distinguish three energy regions for the valence bands. Roughly speaking; The range -6 eV to -10 eV consists of mainly $p$ bands, -10 eV to -14 eV consists of a hybridization of $s$ and $p$ bands, and below that mainly $s$ bands are present. From figure 5.2 we can also identify the bottom of the conduction band as having a $p$-like character. This is consistent with what is found in Ref. [58].

## 5.2 Structural and electronic properties of Ag

**Table 5.4:** Calculated equilibrium lattice constant of bulk Ag, together with calculated value from other work (using the GGA:PW91) and experimental value[a].

| | GGA:PW91 | calc. | expt. |
|---|---|---|---|
| $a$ (Å) | 4.25 | 4.16 | 4.09 |

[a]Experimental value and other GGA:PW91 calculated result was found in Ref. [62, 63].

Calculated equilibrium lattice constant of bulk Ag is presented in table 5.4. Similarly to our calculations on bulk Si the GGA:PW91 functional overshoots the lattice constant experimental value. However the case is more severe for Ag, the overestimate is at 4% relative to experiment, whereas compared to the other calculation it is 2%. As previously discussed the shortcomings of the GGA at predicting bond lengths is evident here as well. And in regards to the mismatch to the other calculated result, it is likely to be a consequence of the fact that the other calculation utilized a plane-wave basis set and ultra-soft pseudopotentials, whilst our calculation utilized STOs and NOs as basis and a small frozen core approximation.

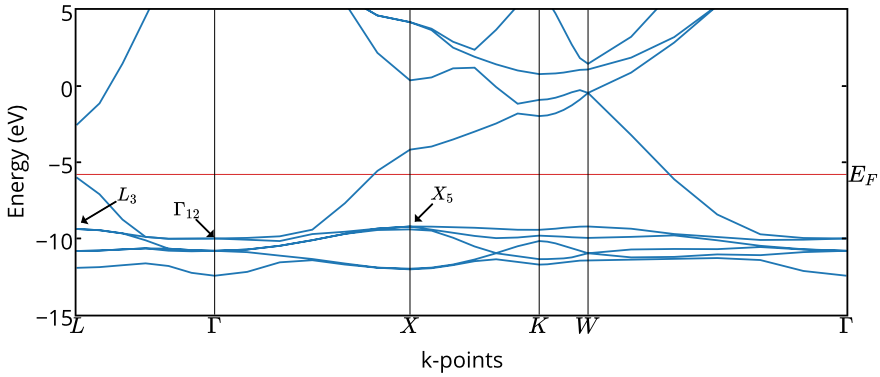


**Figure 5.3:** Calculated band structure of Ag, obtained at the GGA:PW91 equilibrium lattice constant. Labeling of points is done according to Ref. [64].

The calculated electronic band structure of Ag obtained at the GGA:PW91 equilibrium lattice constant ($a = 4.25$ Å) is presented in figure 5.3. The band structure correctly displays the nature of Ag as being a metal, with the Fermi level located inside the bands. The structure corresponds well with the structure presented in the calculations performed by Fuster et al. in Ref. [64]. The correspondence is to some extent highlighted in table

**Table 5.5:** Selected Ag band structure energy differences relative to the Fermi level, together with calculated results from other work and experimental values[a]. All values are in eV.

| | GGA:PW91 | calc. | expt. |
|---|---|---|---|
| $E_F - E_{\Gamma_{12}}$ | 4.20 | 4.29 | 4.95 |
| $E_F - E_{X_5}$ | 3.42 | 3.20 | 3.97 |
| $E_F - E_{L_3}$ | 3.58 | 3.44 | 4.11 |

[a]Calculated results from other work and experimental values were found in Ref. [64].

5.5 where a comparison of distinct calculated energy differences relative to the Fermi level have been made, together with experimental values. The deviation between our results and the other calculat can be argued to originate from the other calculation applying DFT in the Kohn-Sham local density approximation, whereas we apply it in the generalized gradient approximation. Naturally the differences might also be attributed to other technical aspects of the calculations. Both calculations underestimate energy differences relative to the experimental values (by about 15-20%), which again is a familiar feature of DFT.

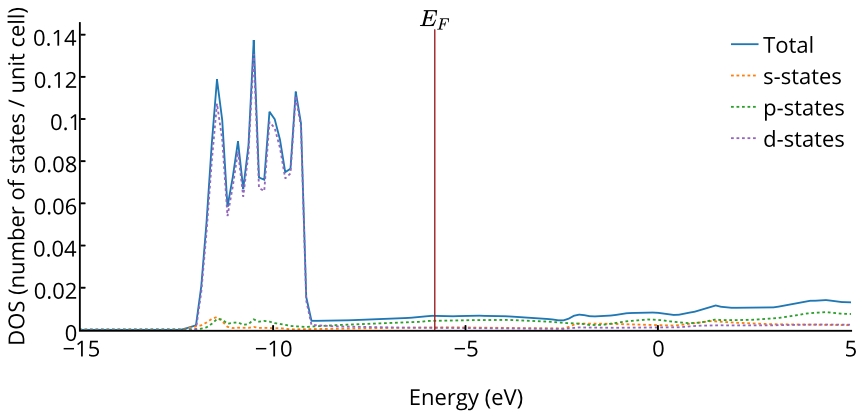


**Figure 5.4:** Calculated density of states with $s$, $p$ and $d$ states contributions for bulk Ag obtained at the GGA:PW91 equilibrium lattice constant.

The calculated electronic density states for bulk Ag obtained at the GGA:PW91 equilibrium lattice constant is presented in figure 5.4. The DOS possesses no band gap at the Fermi level and rightly displays Ag as a metal. A prominent peak consisting of mainly $d$ states below the Fermi level is apparent, and at the Fermi level $p$ states are the major contributor. This agrees well with what has been found in other electronic structure calculations concerning Ag, e.g. those found in Ref. [64, 65].

## 5.3 Ag-doped Si

**DFTB calculations**

Our DFTB calculations have explored the effects of incorporating 2 Ag-atoms in a 16-atom cubic crystal diamond bulk Si 2x2x2 supercell. This yielded a host of possibilities when it came to spacing between the two impurity atoms. By substituting in the two Ag-atoms at different lattice sites, different spacings between them were obtained, and one DFTB calculation was run for each spacing. The geometry optimizations were run without optimization of the lattice, keeping the lattice constant equal to its experimental value $a = 5.43$ Å. The calculations were run as screening calculations looking to see if the emerging results were interesting in terms of the IBSC concept. The resulting DOS profile for each spacing $d$ is presented in figure 5.5, whereas the total density of states for the $d = 940.5$ pm Ag-atoms spacing is highlighted. This result is specifically highlighted due to it being the one exhibiting two most prominent peaks around the Fermi level. Closer inspection also reveals the spacing $d = 543.0$ pm having the same DOS profile as $d = 940.5$ pm. The two prominent peaks are interesting on the basis of the expressed energy levels from Sullivan et al. in Ref. [9], which read; donor level at $E_v + 260$ meV and acceptor level at $E_c - 290$ meV. We briefly discuss these levels before moving onward:

The work cited by Sullivan et al. for these levels is the work by Okuyama et al. in Ref. [66] and the work by Thiel and Ghandhi in Ref. [67]. The work by Okuyama et al. is experimental, and the silver was deposited on n-type Si where the active silver concentration was $9 \times 10^{14}$ cm$^{-3}$. Okuyama et al. do state that their results are in agreement with the energy levels from Thiel and Ghandhi, however it should be noted that they also state that they can not be certain to which band edges their observed energies should be ascribed. The work by Thiel and Ghandhi is also experimental and the donor level at $E_v + 260$ meV was found from p-type samples whilst the acceptor level at $E_c - 290$ meV was found from n-type samples. One p-type sample of $1.1 \times 10^{16}$ cm$^{-3}$ active silver concentration gave donor level at $E_v + 250$ meV, and another sample of $5.5 \times 10^{14}$ cm$^{-3}$ active silver concentration gave donor level at $E_v + 270$ meV, which altogether yielded their $E_v + 260$ meV donor level, with a 0.01 eV uncertainty in their determination. The acceptor level was from n-type samples of $2.4 \times 10^{15}$ cm$^{-3}$ and $1.5 \times 10^{15}$ cm$^{-3}$ active silver concentrations, both giving the energy level at $E_c - 290$ meV.

With these energy level values in mind the two prominent peaks from the highlighted Ag-atoms spacing of $d = 940.5$ pm were of particular interest. And on the basis of that interest the configuration was chosen to be evaluated by the more accurate method of DFT. The DOS and band structure result from the corresponding DFT calculation is shown in figure 5.6. The DOS exhibited from DFT is different from that of DFTB, the two prominent peaks are no longer so distinct and have "smeared" out into valence band and conduction band, leaving no indication of any intermediate bands. This is also evident from the band structure, with bands extending throughout the whole width of the band gap.

This outcome of disagreement between DFTB and DFT results is important here as the main approach for getting a proper accuracy estimate for our DFTB calculations is comparing against a more accurate reference method (DFT). With the level of differences found from just inspecting the DOS from the two methods (from figure 5.5 and figure 5.6), we find DFTB as being not very accurate, and we emphasize that its predictions should be

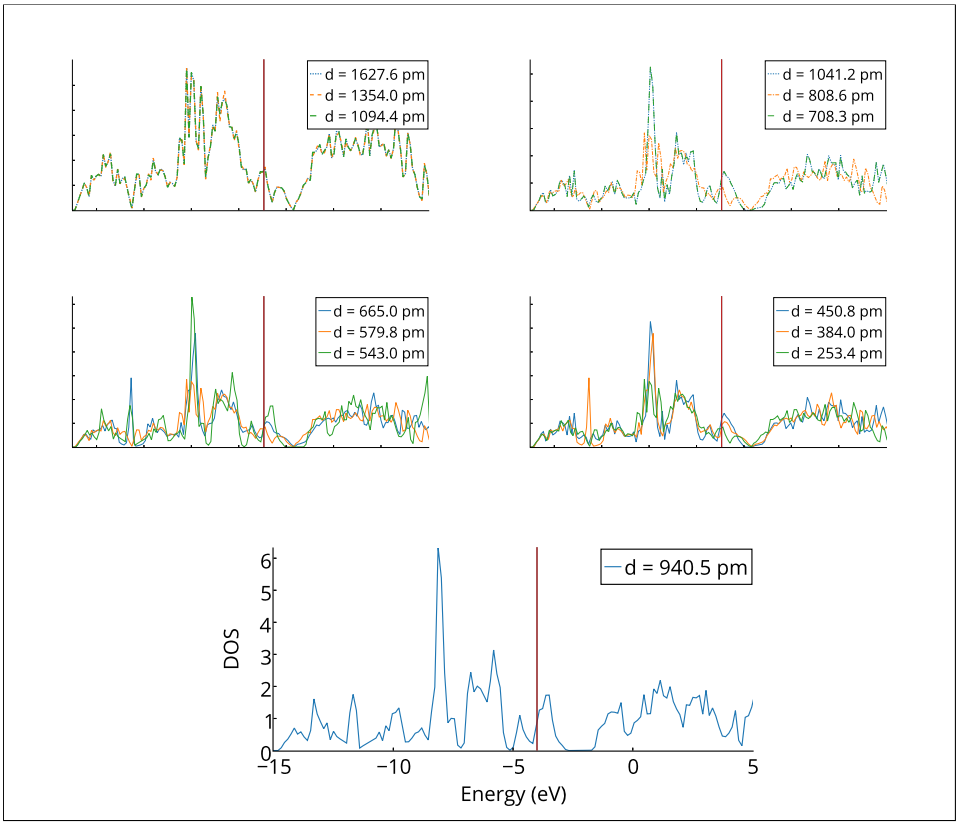


**Figure 5.5:** Total DOS profile overview for different atomic spacings $d$ between the two impurity Ag-atoms in a 16-atom supercell. Fermi level represented by red vertical line.

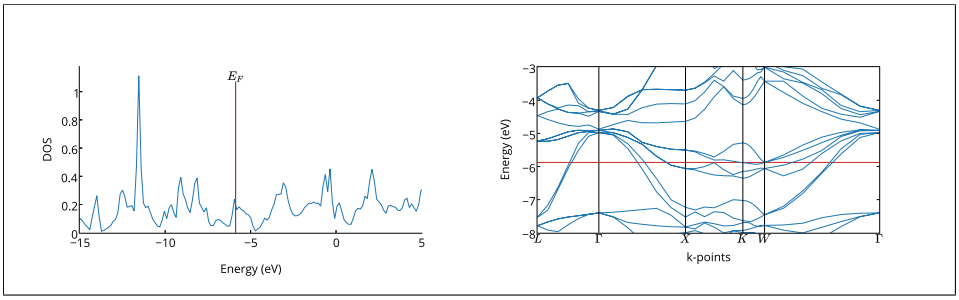


**Figure 5.6:** DFT calculated DOS and band structure for $d = 940.5$ pm impurity Ag-atoms spacing.

examined by more accurate methods.

It is probable that the inadequate accuracy of our DFTB calculations comes from the fact that DFTB has mostly been targeting organic and biological systems. Because of this, DFTB is lacking parameter sets for transition metal elements adjusted for the types of calculations performed in this thesis. Our parameter set "*mio-0-1 + hyb-0-2*", partly stems from studies of adsorption of perylenetetracarboxylic dianhydride (PTCDA) on silver and silicon surfaces. Hence it is not necessarily so that it will work well with our bulk calculations.

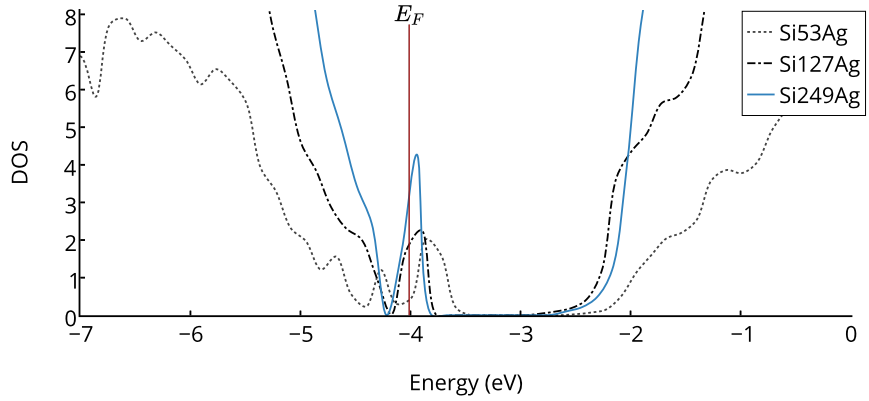


**Figure 5.7:** DOS for Ag-doped Si with 1.85%, 0.78% and 0.40% Ag-impurity concentration.

DFTB calculations were performed to investigate the effects of decreasing the Ag-impurity concentration. This was done by increasing the size of the supercell to 3x3x3, 4x4x4 and 5x5x5 yielding concentrations of 1.85%, 0.78% and 0.40% respectively. In all cases one Si-atom in the supercell was replaced by one Ag-atom, hence these configurations are also denoted by Si53Ag, Si127Ag and Si249Ag, which is the convention used in the presented results in figure 5.7. Figure 5.7 displays the DOS for the different configurations with special regards for what is happening around the Fermi level and band gap. The DOS shows that as the concentration of Ag-impurities goes down, a clear peak in the DOS is emerging at the Fermi level close to the valence band edge. This indicates the formation of a partially filled intermediate band inside the band gap of silicon by Ag-doping at lower concentrations. The band structure of the Si249Ag configuration is shown in figure 5.8. The band structure reveals an intermediate band at the Fermi level which corresponds to the peak in the DOS from figure 5.7.

Some of the IB properties found for the Si249Ag configuration can be read of figure 5.9, which shows an expanded view of the DOS from figure 5.8. Here it is revealed that the "size" of the IB is relatively small, that is, the height of the IB peak is small compared to the peaks in VB and CB (with peak ratios ${}^{\mathrm{IB}}/_{\mathrm{VB}} = 0.11$ and ${}^{\mathrm{IB}}/_{\mathrm{CB}} = 0.13$). This small size is unfavorable in terms of the amount of states available for yielding sub-band gap absorption of photons in IBSCs. The position of the IB is found to be at $E_v + 0.28$ eV,

which corresponds well with the experimental energy level at $E_v + 0.26$ eV for Ag-in-Si previously discussed. And from the band structure the width of the IB is found to be at its maximum at the L-point, where the width reads 0.16 eV. The position of the IB at 0.28 eV above the valence band edge is to some degree encouraging with respect to research indicating the optimum position of an IB being approximately 1/3 of the band gap above VB or below CB, as in Ref. [68]. However, as stated in Ref. [69], predictions by DFT on positions and widths of IBs are not reliable, and as DFTB is an approximate DFT method, our results are not reliable either. No suitable work for comparison of our calculated IB properties were found. We stress here the inaccuracy of our DFTB calculations and emphasize that the IB properties given here should be examined by more accurate methods. The properties are more serving as to give some ideas of what to expect when going to lower concentrations of Ag-impurities in similar computational work, rather than being properties bearing any substantial theoretical weight on their own.

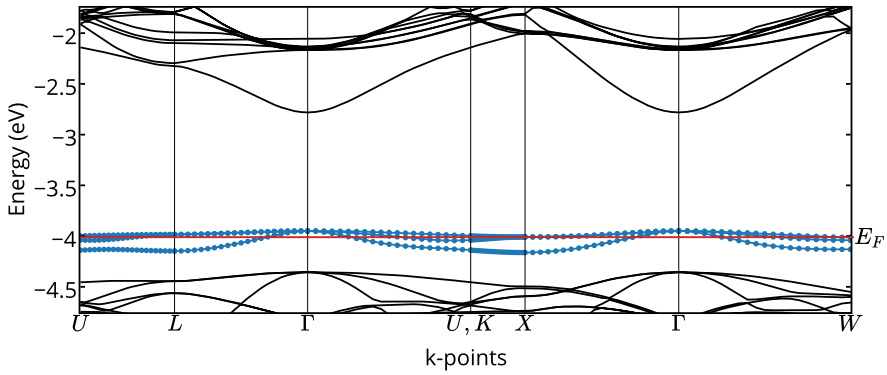


**Figure 5.8:** Band structure for Ag-doped Si at 0.40% impurity concentration.

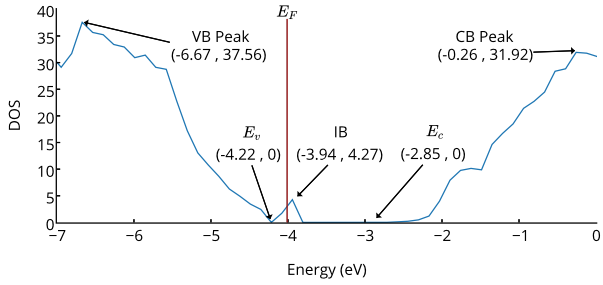


**Figure 5.9:** DOS for Ag-doped Si at 0.40% impurity concentration.

### DFT calculations

A stepwise decrease of Ag-impurity concentration was investigated by generating supercells of increasing size in one direction and substituting one Si-atom with an Ag-atom. This yielded somewhat special configurations with atom-thick planes of silver between layers of silicon. All calculations except the Si7Ag and Si9Ag cases were run with an optimization of the lattice. The resulting total DOS from these DFT calculations are found in figure 5.10. The DOS shows that as the Ag concentration goes down, two peaks are starting to emerge around the Fermi level. These contours are reminiscent of the reports from other work, indicating two energy levels inside the band gap of silicon when doped with silver.

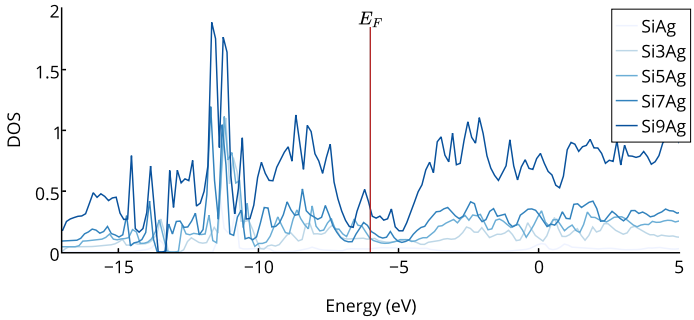


**Figure 5.10:** DOS for Ag-doped Si with 50%, 25%, 16.6%, 12.5% and 10% impurity concentration. The Fermi level displayed is that of the Si9Ag configuration.

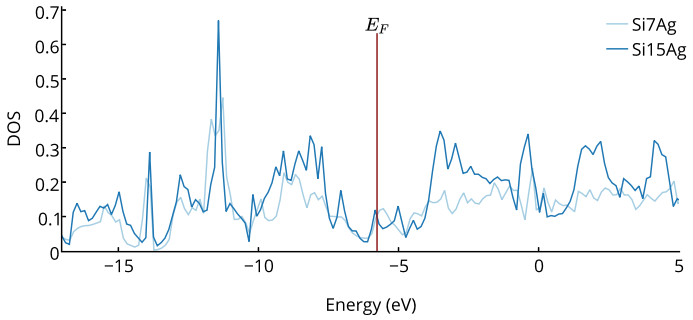


**Figure 5.11:** DOS for Ag-doped Si at 12.5% and 6.25% impurity concentration, in 2x2x1 and 2x2x2 supercell configurations respectively. The Fermi level displayed is that of the S15Ag configuration.

DFT calculations were also run for 2x2x1 and 2x2x2 supercells, yielding Ag-impurity concentrations of 12.5% and 6.25% respectively. The calculations were run without opti-

mization of the lattice. The total DOS from these calculations are shown in figure 5.11. From the DOS it seems evident that the one peak around the Fermi level apparent at 12.5% impurity concentration is splitting in to two peaks when the concentration is lowered to 6.25%. This is rather interesting with regard to what was reported by Castán et al. in Ref. [70]. Castán et al. reported deep levels in titanium-doped silicon moving deeper as the titanium concentration was increased. Similarly this might also be the case for Ag-doped Si here, with the two peaks at 6.25% impurity concentration moving deeper as the concentration is increased and coming together to form one peak at 12.5% impurity concentration. This also gives some indication of more individually localized peaks in the density of states around the Fermi level inside the band gap of silicon when going to lower impurity concentrations, which in turn will hint at the formation of intermediate bands at lower concentrations.

A DFT calculation with optimization of the lattice was run on the 2x2x2 supercell configuration with 6.25% impurity concentration. The equilibrium lattice constant was found to be $a = 5.50$ Å. The band structure and the DOS with PDOS are shown in figures 5.12 and 5.13 respectively. As can be seen from the band structure, there is no formation of intermediate bands at this impurity concentration, the electronic bands are extending throughout the whole width of the band gap. This is also evident from the density of states, with states present everywhere in the band gap, leaving no gap at all, and no intermediate bands. From the PDOS it is apparent that the bands inside the band gap are mostly due to $p$ states from the Si atoms, with a small contribution from Ag $p$ states. Whilst the $d$ states from the Ag atoms are contributing more deeper down in the valence band around -10 eV to -12 eV. This characterization of orbital contributions to the bands are given as to have some indication of what states might contribute to intermediate bands maybe found in further work.

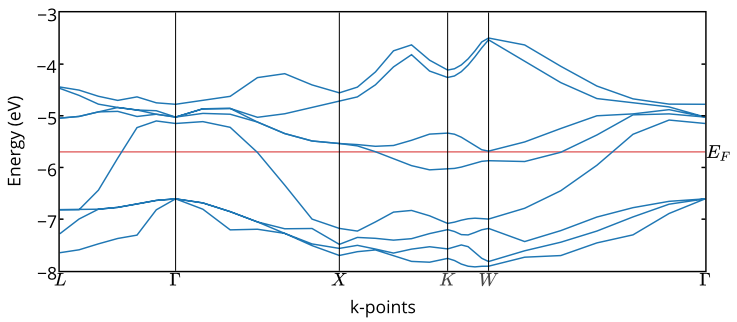


**Figure 5.12:** Band structure for Ag-doped Si at 6.25% impurity concentration

Lastly, we note that although our research on silver doped silicon have particularly taken into account the energy levels expressed by Sullivan et al. in Ref. [9], there have been other energy levels reported. The focus on the donor level at $E_v + 0.26$ eV and acceptor level at $E_c - 0.29$ eV have to some degree been due to the developed estimate of a figure of merit for IBSCs with respect to these levels. However, we bring attention to

the fact that the work found in references [69, 71, 72, 73, 74] all refer to the levels found by Baber et al. in Ref. [75], which are at $E_v + 0.34$ eV and $E_c - 0.54$ eV. And we also note the levels; ($E_v + 0.37$ eV and $E_c - 0.29$ eV), ($E_v + 0.41$ eV and $E_c - 0.59$ eV), ($E_v + 0.33$ eV and $E_c - 0.36$ eV) and ($E_v + 0.29$ eV and $E_c - 0.62$ eV) which are all cited by Fazzio et al. in Ref. [76].

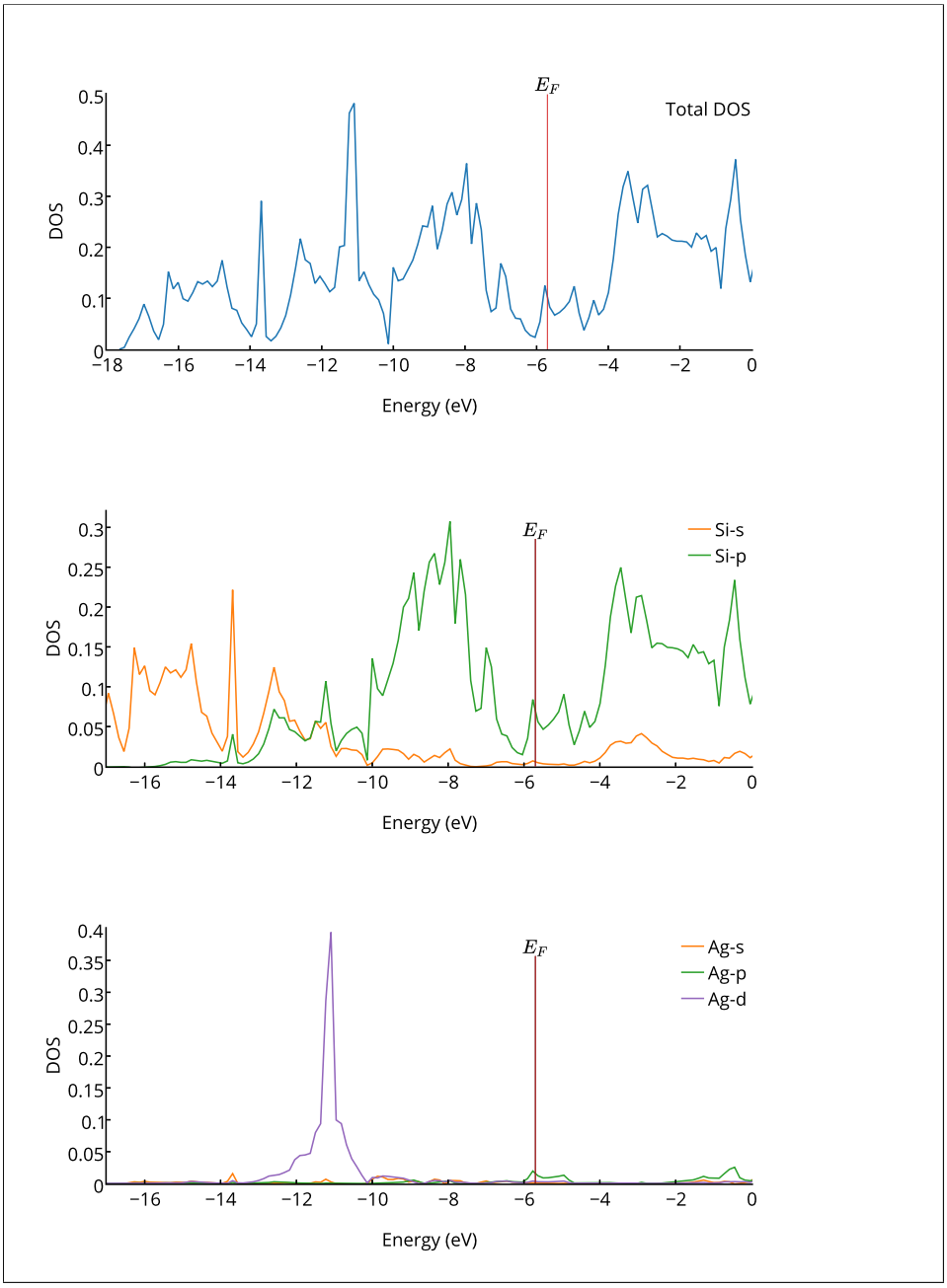


**Figure 5.13:** Calculated DOS of Ag-doped Si at 6.25% impurity concentration.

## 5.4 3d transition metal doping of Si

The doping of Si by transition metals of the 3d series was explored by DFT. The supercell size was 2x2x2 and one Si-atom was substituted by a transition metal atom at its lattice site. The impurity concentration was 6.25% in all calculations. All calculations were run with an optimization of the lattice, except for Cr-doping (due to time limitation). Band structures and DOS with PDOS were obtained at the calculated equilibrium lattice constant. The calculated equilibrium lattice constants are summarized in table 5.6.

**Table 5.6:** Impurity effects on lattice constant.

| | Si:V | Si:Cr | Si:Mn | Si:Fe | Si:Co |
|---|---|---|---|---|---|
| $a$ (Å) | 5.48 | - | 5.45 | 5.43 | 5.43 |

We bring attention to the fact the our results are from the transition metal impurities occupying substitutional site in bulk Si cubic crystal diamond structure. Zhang et al. in Ref. [77] found that $3d$ TM impurities prefer interstitial site with hexagonal symmetry in bulk Si. However, it is also found that an applied pressure can stabilize the substitutional position of $3d$ TM impurities in Si. It is also evident from Ref. [77] that a Zinc blende and/or B20 structure would have been more appropriate for our calculations. We also bring attention to IB properties having been reported for the doping of silicon by our $3d$ transition metals Cr and Fe, in a poorly documented article found in Ref. [78].

We state already here that our results show no complete intermediate band formed by the $3d$ TM doping. We point out that our results are all from one specific impurity concentration and that calculations carried out over a greater range of concentrations, in a more suitable structure, would have led to more significance. We present our results with regard to give some insight into how bands around the Fermi level appears in the band structure, and how $s$, $p$ and $d$ states are contributing.

### 5.4.1 V-doped Si

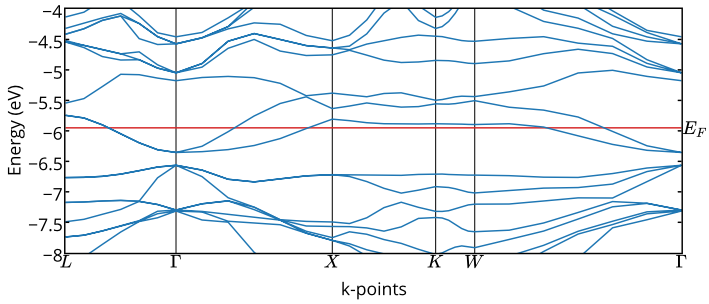


**Figure 5.14:** Band structure for V-doped Si at 6.25% impurity concentration.

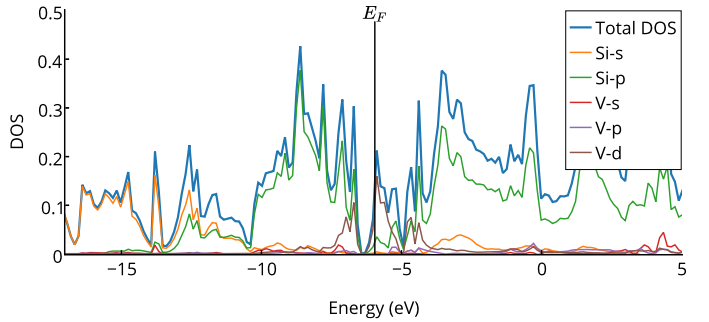


**Figure 5.15:** DOS for V-doped Si at 6.25% impurity concentration.

Band structure and DOS is shown in figures 5.14 and 5.15 respectively. A very wide (almost the full width of the gap) intermediate band might seem present in the band structure. However, closer inspection of the DOS reveals that DOS is not zero at the conduction band edge, yielding no intermediate band. Nonetheless, these contours are quite promising with strong contributions from vanadium $d$ states at the Fermi level, and some contribution from silicon $p$ states. It seems evident from the DOS that the two-peak region inside the band gap have mainly V-$d$ state contributions in the strongest peak closest to the Fermi level, whereas Si-$p$ are contributing stronger to the smaller peak closer to the conduction band, meaning the bands closer to the Fermi level will have more of a $d$-like character.

### 5.4.2 Cr-doped Si

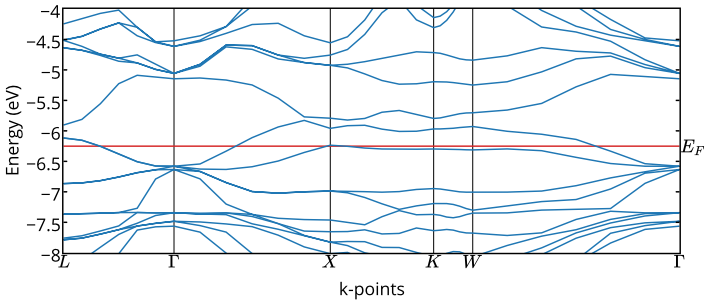


**Figure 5.16:** Band structure for Cr-doped Si at 6.25% impurity concentration.

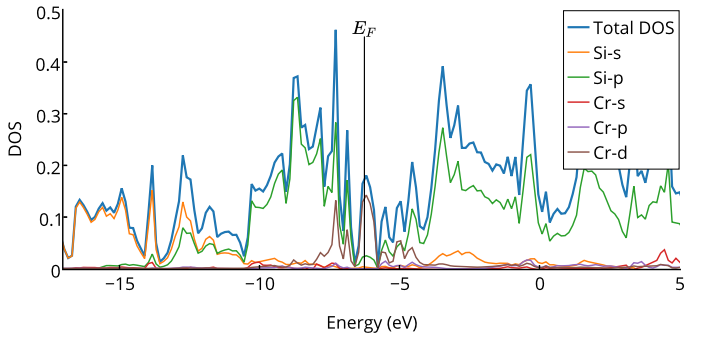


**Figure 5.17:** DOS for Cr-doped Si at 6.25% impurity concentration.

Band structure and DOS is shown in figures 5.16 and 5.17 respectively. The DOS exhibits a strong peak at the Fermi level, mostly from chromium $d$ states and a little contribution from silicon $p$ states. The peak is not fully individually localized, with small, but finite amount of states at its edges. Accordingly, no intermediate band is found. Also, a triple peak of increasing size in the direction of increasing energy is found around -5 eV consisting of chromium $d$ states and silicon $p$ states. All these peaks in density of states can be of interest to the formation of intermediate bands at other Cr-impurity concentrations. The bands in the band structure found inside the region of where pure silicon has its band gap are mainly consisting of Cr-$d$ states and Si-$p$ states. The Cr-$d$ state contribution is primarily inside the -8 eV to -4 eV region, whilst Cr $s$ and $p$ states do not seems to contribute much to the bands at all.

### 5.4.3 Mn-doped Si

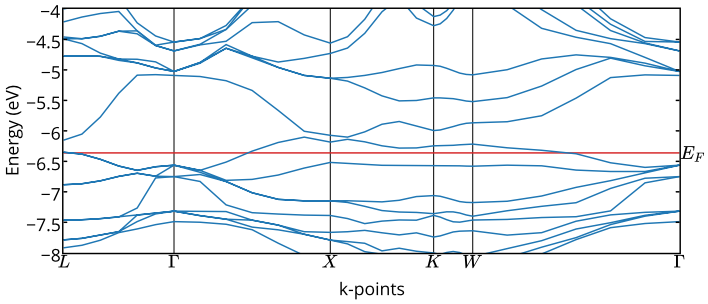


**Figure 5.18:** Band structure for Mn-doped Si at 6.25% impurity concentration.

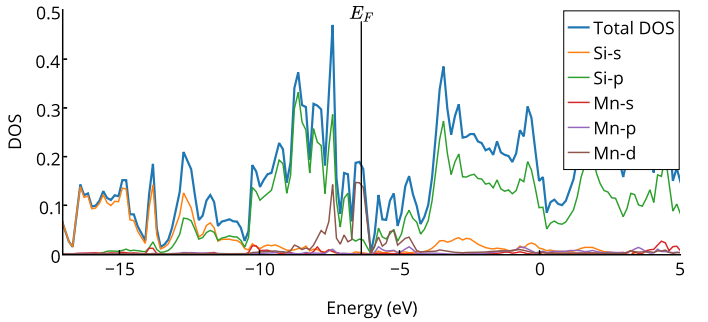


**Figure 5.19:** DOS for Mn-doped Si at 6.25% impurity concentration.

Band structure and DOS is shown in figures 5.18 and 5.19 respectively. By comparison to the case of Cr-doped Si the result of Mn-doped Si is very similar. The profiles of both band structures and DOS are very much alike and we refer to the previous discussion in subsection 5.4.2 for how different states are contributing to bands at different energies. We only note that for the Mn-doping case compared to the Cr-doping, the peaks in the DOS to immediately lower and higher energies around the Fermi level seems to have widened down. Indicating that the Mn-doping of Si gives rise to more outspread energy levels at these locations compared to Cr-doping.

### 5.4.4 Fe-doped Si

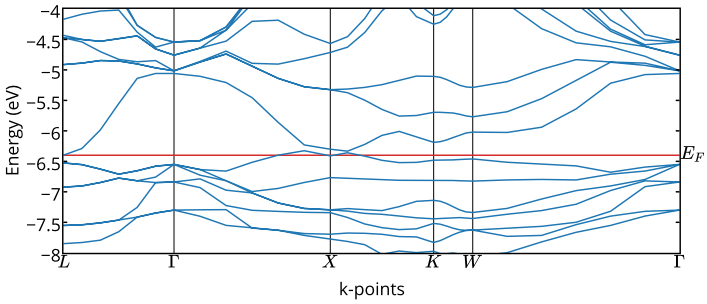


**Figure 5.20:** Band structure for Fe-doped Si at 6.25% impurity concentration.

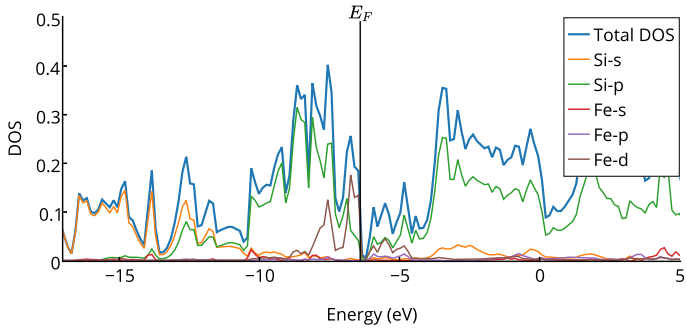


**Figure 5.21:** DOS for Fe-doped Si at 6.25% impurity concentration.

Band structure and DOS is shown in figures 5.20 and 5.21 respectively. Again, the case is similar to the ones of Cr and Mn doping. No intermediate band is found and the bands which have formed inside the band gap appear to be due to a hybridization of Si-$p$ states and $d$ states originating from the dopant atoms.

### 5.4.5 Co-doped Si

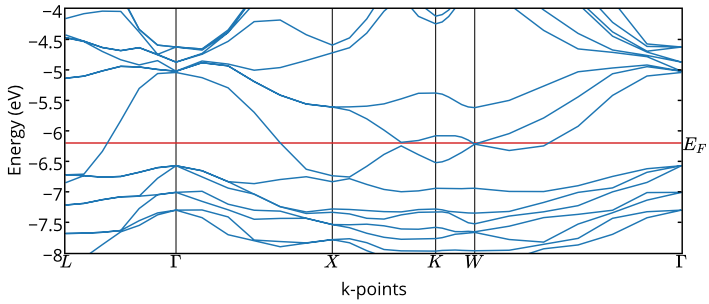


**Figure 5.22:** Band structure for Co-doped Si at 6.25% impurity concentration.

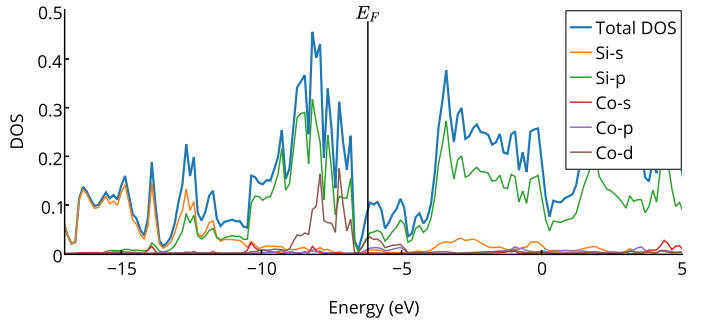


**Figure 5.23:** DOS for Co-doped Si at 6.25% impurity concentration.

Band structure and DOS is shown in figures 5.22 and 5.23 respectively. From the band structure it is evident that bands have formed inside the band gap of silicon. However, the bands extend throughout the entire gap and are thereby not suitable as intermediate bands for the IBSC concept. The lack individually localized intermediate bands within the band gap of silicon is also evident from the density of states, with states present at all energies. The $d$ states of the Co-atoms appear to have their contribution mainly to bands in the -10 eV to -5 eV energy region. Silicon $p$ states are present and contributing to bands above -15 eV. And Si-$s$ states are principally contributing outside the region of interest for intermediate band formation (below -10 eV and above -4.5 eV), which has been the impression also in our previous results for $3d$ TM doping.

Chapter 6

# Conclusions

In summary, we conducted DFT and DFTB calculations to study the formation of intermediate bands when silicon is doped with a transition metal impurity. Initial results revealed the typical shortcomings of our DFT method with regards to band gap predictions. Which in turn have highlighted the fact that predictions made on the positioning of intermediate bands can be questionable. Structural and electronic properties of silicon and silver have appeared to agree well with other theoretical work. From DFTB density of states and band structure we have found that substitutional doping of cubic crystal diamond bulk Si doped with silver at 0.4% impurity concentration, exhibits an intermediate band at the Fermi level, 0.28 eV above the valence band edge, corresponding well with an experimentally predicted energy level at 0.26 eV above the valence band edge. On the other hand, we have also found that our DFTB calculations do not possess desired accuracy, and that its results should not be taken to bear too much theoretical weight without proper cross-examination by a more accurate method. DFT results have revealed only contours of intermediate band formation for silver-doped silicon down to 6.25% impurity concentration. The bands formed inside the gap have been shown to mostly come from silicon $p$ states. The doping of silicon by the $3d$ series V, Cr, Mn, Fe and Co at 6.25% impurity concentration, was shown to produce bands inside the band gap mainly consisting of hybridizations of Si-$p$ states and dopant-$d$ states. However, no fully formed intermediate bands were found.

Chapter 7

# Future work

Possible further lines of study based on the work presented in this thesis are manifold. A more extensive literature review of the research already conducted on transition metal doping of silicon would be of great value. Thorough convergence tests on the results which have been presented can be conducted. Seeing how the results come out by applying other exchange-correlation functionals, various basis sets and setting different convergence criteria is especially needed. Running first-principles calculations on different impurity concentrations is of particular interest, especially in terms of investigating the DFTB predicted intermediate band formed by the doping of silicon with silver. Other transition metal impurities in silicon can be examined. The effects of vacancies and dopant-to-dopant interactions can be considered. And also, entirely different effects which might produce materials suitable for intermediate band solar cells can be studied.

# Bibliography


[1] A. Luque and A. Martí, "Increasing the efficiency of ideal solar cells by photon induced transitions at intermediate levels," *Physical Review Letters*, vol. 78, no. 26, p. 5014, 1997.

[2] Y. Okada, N. Ekins-Daukes, T. Kita, R. Tamaki, M. Yoshida, A. Pusch, O. Hess, C. Phillips, D. Farrell, K. Yoshida, *et al.*, "Intermediate band solar cells: Recent progress and future directions," *Applied Physics Reviews*, vol. 2, no. 2, p. 021302, 2015.

[3] A. Luque and A. Martí, "The intermediate band solar cell: progress toward the realization of an attractive concept," *Advanced Materials*, vol. 22, no. 2, pp. 160–174, 2010.

[4] P. Siffert and E. Krimmel, *Silicon: Evolution and future of a technology*. Springer Science & Business Media, 2013.

[5] M. A. Green, *Solar Cells - Operating Principles, Technology and Systems Applications*. The University of New South Wales, 1998.

[6] W. Shockley and H. J. Queisser, "Detailed balance limit of efficiency of p-n junction solar cells," *Journal of applied physics*, vol. 32, no. 3, pp. 510–519, 1961.

[7] K. Lu, *Materials in Energy Conversion, Harvesting, and Storage*. John Wiley & Sons, 2014.

[8] A. Luque, A. Martí, and C. Stanley, "Understanding intermediate-band solar cells," *Nature Photonics*, vol. 6, no. 3, pp. 146–152, 2012.

[9] J. T. Sullivan, C. B. Simmons, T. Buonassisi, and J. J. Krich, "Targeted search for effective intermediate band solar cell materials," *Photovoltaics, IEEE Journal of*, vol. 5, no. 1, pp. 212–218, 2015.

[10] D. S. Sholl and J. A. Steckel, *Density functional theory - A practical introduction*. Wiley, 2009.

[11] E. Schrödinger, "Quantisierung als eigenwertproblem," *Annalen der physik*, vol. 385, no. 13, pp. 437–490, 1926.

[12] M. Born and R. Oppenheimer, "Zur quantentheorie der molekeln," *Annalen der Physik*, vol. 389, no. 20, pp. 457–484, 1927.

[13] D. R. Hartree, "The wave mechanics of an atom with a non-coulomb central field. part i. theory and methods," in *Mathematical Proceedings of the Cambridge Philosophical Society*, vol. 24, pp. 89–110, Cambridge Univ Press, 1928.

[14] W. Pauli, "Über den zusammenhang des abschlusses der elektronengruppen im atom mit der komplexstruktur der spektren," *Zeitschrift für Physik A Hadrons and Nuclei*, vol. 31, no. 1, pp. 765–783, 1925.

[15] W. Pauli, "Nobel lecture," *Nobel Lectures, Physics*, pp. 1942–1962, 1946.

[16] V. Fock, "Selfconsistent field mit austausch für natrium," *Zeitschrift für Physik*, vol. 62, no. 11-12, pp. 795–805, 1930.

[17] J. C. Slater, "The theory of complex spectra," *Physical Review*, vol. 34, no. 10, p. 1293, 1929.

[18] J. Thijssen, *Computational physics*. Cambridge University Press, 2007.

[19] D. A. McQuarrie, *Quantum chemistry*. University Science Books, 2008.

[20] A. R. Leach, *Molecular modelling: principles and applications*. Pearson education, 2001.

[21] M. P. Marder, *Condensed matter physics*. John Wiley & Sons, 2010.

[22] G. Grosso and G. P. Parravicini, *Solid State Physics*. Academic Press, 2013.

[23] L. H. Thomas, "The calculation of atomic fields," in *Mathematical Proceedings of the Cambridge Philosophical Society*, vol. 23, pp. 542–548, Cambridge Univ Press, 1927.

[24] E. Fermi, "Un metodo statistico per la determinazione di alcune priorieta dell'atome," *Rend. Accad. Naz. Lincei*, vol. 6, no. 602-607, p. 32, 1927.

[25] B. Santra, *Density-functional theory exchange-correlation functionals for hydrogen bonds in water*. PhD thesis, Technische Universität Berlin Berlin, 2010.

[26] P. Hohenberg and W. Kohn, "Inhomogeneous electron gas," *Physical review*, vol. 136, no. 3B, p. B864, 1964.

[27] W. Kohn and L. J. Sham, "Self-consistent equations including exchange and correlation effects," *Physical Review*, vol. 140, no. 4A, p. A1133, 1965.

[28] J. P. Dahl, *Introduction to the quantum world of atoms and molecules*. World Scientific, 2001.

[29] E. Lindholm and L. Asbrink, *Molecular orbitals and their energies, studied by the semiempirical HAM method*, vol. 38. Springer Science & Business Media, 2012.

[30] E. G. Lewars, *Computational chemistry: introduction to the theory and applications of molecular and quantum mechanics*. Springer Science & Business Media, 2010.

[31] J. Rychlewski, *Explicitly correlated wave functions in chemistry and physics: theory and applications*, vol. 13. Springer Science & Business Media, 2003.

[32] K. D. Sattler, *Handbook of nanophysics: principles and methods*. CRC press, 2010.

[33] R. G. Parr and W. Yang, *Density-functional theory of atoms and molecules*, vol. 16. Oxford university press, 1989.

[34] P. A. Dirac, "Note on exchange phenomena in the thomas atom," in *Mathematical Proceedings of the Cambridge Philosophical Society*, vol. 26, pp. 376–385, Cambridge Univ Press, 1930.

[35] m. F. Bloch, "Bemerkung zur elektronentheorie des ferromagnetismus und der elektrischen leitfähigkeit," *Zeitschrift für Physik*, vol. 57, no. 7-8, pp. 545–555, 1929.

[36] G. E. Scuseria and V. N. Staroverov, "Progress in the development of exchange-correlation functionals," 2005.

[37] L. Kantorovich, *Quantum theory of the solid state: an introduction*, vol. 136. Springer Science & Business Media, 2004.

[38] R. Dronskowski, *Computational chemistry of solid state materials: a guide for materials scientists, chemists, physicists and others*. John Wiley & Sons, 2008.

[39] M. Schlesinger, *Modelling and Numerical Simulations II*, vol. 44. Springer Science & Business Media, 2009.

[40] V. Gupta, *Principles and Applications of Quantum Chemistry*. Academic Press, 2015.

[41] M. Swart, F. M. Bickelhaupt and M. Duran, "Density functionals poll," 2013. Available online at www.marcelswart.eu/dft-poll. Accessed November 4, 2015.

[42] E. Scheer, *Molecular electronics: an introduction to theory and experiment*, vol. 1. World Scientific, 2010.

[43] I. Y. Zhang and X. Xu, *A New-Generation Density Functional: Towards Chemical Accuracy for Chemistry of Main Group Elements*. Springer Science & Business Media, 2013.

[44] S. K. Ghosh and P. K. Chattaraj, *Concepts and Methods in Modern Theoretical Chemistry: Electronic Structure and Reactivity*. CRC Press, 2013.

[45] A. D. Becke, "Density-functional exchange-energy approximation with correct asymptotic behavior," *Physical review A*, vol. 38, no. 6, p. 3098, 1988.

[46] J. P. Perdew, P. Ziesche, and H. Eschrig, *Electronic structure of solids' 91*, vol. 11. Akademie Verlag, Berlin, 1991.

[47] J. P. Perdew, K. Burke, and M. Ernzerhof, "Generalized gradient approximation made simple," *Physical review letters*, vol. 77, no. 18, p. 3865, 1996.

[48] J. P. Perdew, J. Chevary, S. Vosko, K. A. Jackson, M. R. Pederson, D. Singh, and C. Fiolhais, "Atoms, molecules, solids, and surfaces: Applications of the generalized gradient approximation for exchange and correlation," *Physical Review B*, vol. 46, no. 11, p. 6671, 1992.

[49] C. Lee, W. Yang, and R. G. Parr, "Development of the colle-salvetti correlation-energy formula into a functional of the electron density," *Physical review B*, vol. 37, no. 2, p. 785, 1988.

[50] W. Tress, *Organic Solar Cells*. Springer, 2014.

[51] D. Vasileska, S. Goodnick, and G. Klimeck, "Computational electronics: Semiclassical and quantum device modelling and simulation," 2012.

[52] D. Esseni, P. Palestri, and L. Selmi, *Nanoscale MOS transistors: semi-classical transport and applications*. Cambridge University Press, 2011.

[53] "scm.com/product/bandperiodicdft/."

[54] "scm.com/product/dftb/."

[55] P. Koskinen and V. Mäkinen, "Density-functional tight-binding for beginners," *Computational Materials Science*, vol. 47, no. 1, pp. 237–253, 2009.

[56] A. F. Oliveira, G. Seifert, T. Heine, and H. A. Duarte, "Density-functional based tight-binding: an approximate dft method," *Journal of the Brazilian Chemical Society*, vol. 20, no. 7, pp. 1193–1205, 2009.

[57] "http://www.dftb.org/parameters/download/hyb/hyb-0-2/."

[58] C. Fiolhais, F. Nogueira, and M. A. Marques, *A primer in density functional theory*, vol. 620. Springer Science & Business Media, 2003.

[59] H. Xiao, J. Tahir-Kheli, and W. A. Goddard III, "Accurate band gaps for semiconductors from density functional theory," *The Journal of Physical Chemistry Letters*, vol. 2, no. 3, pp. 212–217, 2011.

[60] M. Hortamani, *Theory of adsorption, diffusion and spinpolarization of Mn on Si (001) and Si (111) substrates*. PhD thesis, Freie Universität Berlin, 2006.

[61] M. Grundmann, *The physics of semiconductors: an introduction including devices and nanophysics*. Springer Science & Business Media, 2006.

[62] B. Medasani, Y. H. Park, and I. Vasiliev, "Theoretical study of the surface energy, stress, and lattice contraction of silver nanoparticles," *Physical Review B*, vol. 75, no. 23, p. 235436, 2007.

[63] M.-L. Bocquet, A. Rappe, and H.-L. Dai*, "A density functional theory study of adsorbate-induced work function change and binding energy: Olefins on ag (111)," *Molecular Physics*, vol. 103, no. 6-8, pp. 883–890, 2005.

[64] G. Fuster, J. Tyler, N. Brener, J. Callaway, and D. Bagayoko, "Electronic structure and related properties of silver," *Physical Review B*, vol. 42, no. 12, p. 7322, 1990.

[65] L.-M. Yang, T. Frauenheim, and E. Ganz, "The new dimension of silver," *Physical Chemistry Chemical Physics*, vol. 17, no. 30, pp. 19695–19699, 2015.

[66] M. Okuyama, N. Matsunaga, J. Chen, and A. Milnes, "Photoionization cross-sections and energy levels of gold, iron, platinum, silver, and titanium in silicon," *Journal of Electronic Materials*, vol. 8, no. 4, pp. 501–515, 1979.

[67] F. L. Thiel and S. K. Ghandhi, "Electronic properties of silicon doped with silver," *Journal of Applied Physics*, vol. 41, no. 1, pp. 254–263, 1970.

[68] C. A. R. Linge, "Modeling of the intermediate band tandem solar cell: Using the am1. 5 spectra," 2011.

[69] M. Han, X. Zhang, and Z. Zeng, "The investigation of transition metal doped cugas 2 for promising intermediate band materials," *RSC Advances*, vol. 4, no. 107, pp. 62380–62386, 2014.

[70] H. Castán, E. Pérez, H. García, S. Duenas, L. Bailón, J. Olea, D. Pastor, E. García-Hemme, M. Irigoyen, and G. González-Díaz, "Experimental verification of intermediate band formation on titanium-implanted silicon," *Journal of Applied Physics*, vol. 113, no. 2, p. 024104, 2013.

[71] N. Vinh, M. Klik, and T. Gregorkiewicz, "Time-resolved photoluminescence study of si: Ag," *Physica B: Condensed Matter*, vol. 308, pp. 414–417, 2001.

[72] A. Ali, M. Z. Iqbal, and N. Baber, "Effects of annealing and $\alpha$ irradiation on deep levels in silver-doped n-type silicon," *Journal of applied physics*, vol. 77, no. 7, pp. 3315–3322, 1995.

[73] A. Ali, N. Baber, and M. Z. Iqbal, "Study of deep levels in alpha-irradiated silver-doped p-type silicon," *Journal of applied physics*, vol. 77, no. 10, pp. 5050–5059, 1995.

[74] N. Son, M. Singh, J. Dalfors, B. Monemar, and E. Janzén, "Electronic structure of a photoluminescent center in silver-doped silicon," *Physical Review B*, vol. 49, no. 24, p. 17428, 1994.

[75] N. Baber, H. Grimmeiss, M. Kleverman, P. Omling, and M. Z. Iqbal, "Characterization of silver-related deep levels in silicon," *Journal of applied physics*, vol. 62, no. 7, pp. 2853–2857, 1987.

[76] A. Fazzio, M. Caldas, and A. Zunger, "Electronic structure of copper, silver, and gold impurities in silicon," *Physical Review B*, vol. 32, no. 2, p. 934, 1985.

[77] Z. Zhang, B. Partoens, K. Chang, and F. Peeters, “First-principles study of transition metal impurities in si,” *Physical Review B*, vol. 77, no. 15, p. 155201, 2008.

[78] A. Rostami, H. Heidarzadeh, H. Baghban, M. Dolatyari, and H. Rasooli, “Introducing high efficiency solar cells based on crystalline silicon doped with transition metals,” 2012.

# Appendix A

## A1: Exchange functionals

B88:

$$F_{\mathrm{X}}^{\mathrm{B88}}(s) = \frac{1 + s \cdot a_1 \cdot \sinh^{-1}(s \cdot a_2) + a_3 \cdot s^2}{1 + s \cdot a_1 \cdot \sinh^{-1}(s \cdot a_2)},$$

PW91x:

$$F_{\mathrm{X}}^{\mathrm{PW91}}(s) = \frac{1 + s \cdot a_1 \cdot \sinh^{-1}(s \cdot a_2) + \left(a_3 - a_4 \cdot e^{-100s^2}\right)s^2}{1 + s \cdot a_1 \cdot \sinh^{-1}(s \cdot a_2) + a_5 \cdot s^4},$$

PBEx:

$$F_{\mathrm{X}}^{\mathrm{PBE}}(s) = 1 + a_6 - \frac{a_6}{\left(1 + \frac{a_7}{a_6}s^2\right)}.$$

Here, the parameters in the above equations are:

$$a_1 = 0.19645, \qquad a_2 = \left(48\pi^2\right)^{1/3}, \qquad a_3 = -\frac{a_2^2}{2^{1/3} \cdot \left(-\frac{3}{4}\left(\frac{3}{\pi}\right)^{1/3}\right)} \cdot 0.0042,$$

$$a_4 = \frac{10}{81} - a_3, \qquad a_5 = \frac{-a_2^4 \cdot 10^{-6}}{2^{1/3} \cdot \left(-\frac{3}{4}\left(\frac{3}{\pi}\right)^{1/3}\right)}, \qquad a_6 = 0.804, \qquad a_7 = 0.21951.$$

# A2: Correlation functionals

PBEc:

$$E_{\mathrm{C}}^{\mathrm{PBE}} = \int n(\mathbf{r}) \left( \epsilon_{\mathrm{C}}^{\mathrm{LDA:PW}} + g^3 \frac{\beta^2}{2\alpha} \ln \left[ 1 + \frac{2\alpha}{\beta} \frac{t^2 + At^4}{1 + At^2 + A^2 t^4} \right] \right) \mathrm{d}\mathbf{r}$$

PW91c:

$$E_{\mathrm{C}}^{\mathrm{PW91}} = \int n(\mathbf{r}) \left( \epsilon_{\mathrm{C}}^{\mathrm{LDA:PW}} + g^3 \frac{\beta^2}{2\alpha'} \ln \left[ 1 + \frac{2\alpha'}{\beta} \frac{t^2 + A't^4}{1 + A't^2 + A'^2 t^4} \right] + \left( \frac{16}{\pi} \right) (3\pi^2)^{1/3} \left[ C_c(r_s) - C_c(0) - \frac{3C_x}{7} \right] g^3 t^2 \exp \left[ -100 g^4 t^2 \left( \frac{k_s^2}{k_F^2} \right) \right] \right) \mathrm{d}\mathbf{r}$$

with parameters:

$$A = \frac{2\alpha}{\beta} \left( \exp \left[ \frac{-2\alpha \epsilon_{\mathrm{C}}^{\mathrm{LDA:PW}}}{g^3 \beta^2} \right] - 1 \right)^{-1}, \qquad A' = \frac{2\alpha}{\beta} \left( \exp \left[ \frac{-2\alpha' \epsilon_{\mathrm{C}}^{\mathrm{LDA:PW}}}{g^3 \beta^2} \right] - 1 \right)^{-1}$$

$$\alpha = 0.0716, \qquad \alpha' = 0.09, \qquad \beta = 0.066725,$$

$$t = \frac{|\boldsymbol{\nabla} n(\mathbf{r})|}{2 g k_s n(\mathbf{r})}, \qquad k_s = \left( \frac{4 k_F}{\pi} \right)^{1/2}, \qquad k_F = \left( 3\pi^2 n(\mathbf{r}) \right)^{1/3}$$

$$g = \frac{1}{2} \Big[ (1+\xi)^{2/3} + (1-\xi)^{2/3} \Big], \qquad \xi = \frac{n_\alpha(\mathbf{r}) - n_\beta(\mathbf{r})}{n_\alpha(\mathbf{r}) + n_\beta(\mathbf{r})},$$

$C_c =$ Rasolt and Geldart constants, $\quad r_s =$ Wigner-Seitz radius, $\quad C_x =$ Sham coefficient,

$\epsilon_{\mathrm{C}}^{\mathrm{LDA:PW}} =$ Perdew-Wang parametrization of quantum Monte Carlo simulations for uniform electron gas,

$t =$ scaled density gradient, $\quad g =$ spin-scaling factor

$\xi =$ relative spin-polarization, $\quad n_\alpha$ and $n_\beta =$ spin-densities

$k_s =$ Thomas-Fermi screening wave vector, $\quad k_F =$ local Fermi wave vector

LYP:

$$E_{\mathrm{C}}^{\mathrm{LYP}} = -a \int \frac{1}{1 + dn(\mathbf{r})^{-1/3}} \Bigg[ \mathbf{r} + bn(\mathbf{r})^{-2/3} \Bigg( C_F n(\mathbf{r})^{5/3} - 2t_w + \left( \frac{1}{9} t_w + \frac{1}{18} \nabla^2 n(\mathbf{r}) \right) e^{-cr^{-1/3}} \Bigg) \Bigg] \mathrm{d}\mathbf{r}$$

with parameters:

$$t_w(\mathbf{r}) = \sum_{i=1}^{N} \frac{|\boldsymbol{\nabla} n_i(\mathbf{r})|^2}{n_i(\mathbf{r})} - \frac{1}{8} \nabla^2 n(\mathbf{r}) \qquad C_F = \frac{3}{10} \left(3\pi^2\right)^{2/3}$$

$$a = 0.049 \qquad b = 0.132 \qquad c = 0.2533 \qquad d = 0.3490$$